Title	Computational Photography based on 8-D Reflectance Field
Author(s)	Tagawa, Seiichi
Citation	大阪大学, 2013, 博士論文
Version Type	VoR
URL	https://hdl.handle.net/11094/27478
rights	
Note	

Computational Photography
based on 8-D Reflectance Field

January 2013

Seiichi TAGAWA

Computational Photography
based on 8-D Reflectance Field

Submitted to
Graduate School of Information Science and Technology
Osaka University

January 2013

Seiichi TAGAWA

Abstract

The appearance of an object depends on its reflectance. Here, appearances depend on the reflectance, illumination, and observation. Of the three factors that control appearance, reflectance is the most difficult to deal with. An eight-dimensional reflectance field can completely represent an appearance consisting of the reflectances of objects, illumination, observation, and interreflections between objects. However, because of the high dimensionality, 8-D reflectance fields have not been developed.

To realize practical use of an 8-D reflectance field, I have designed a measuring system, a computing framework, and a rapid measurement method for a 4-D reflectance field and applied them practically.

In designing the system, one of the important issues is how to uniformly deal with the rays in a scene. Ideally, many projectors and cameras should be placed spherically around the target scene. However, such a system is infeasible. So, I developed a polyhedral mirror named the turtleback reflector, exploiting characteristics of an ellipsoid and geodesic domes that are approximately regular polyhedrons. Combining the turtleback reflector with a projector and camera, many virtual projectors and cameras can be placed uniformly but sparsely on a hemisphere. Doing this makes it possible to measure entire 8-D reflectance fields.

Next, I solved the problem of there being no computing framework for 8-D reflectance fields. I have proposed a framework for imaging with 8-D reflectance fields that unifies various individual computational photography techniques. Here, I show the formulations of three computational photography techniques in my framework and the computational result using my system with the turtleback reflector.

Another problem is the measuring time of reflectance fields. Measuring time is very long even for a 4-D reflectance field because although the light reflected in various directions can be captured at the same time, we cannot simply illuminate the scene in various directions to acquire reflected light for each illumination. Accordingly, I have developed a method for rapidly measuring reflectance properties in 4-D reflectance fields. This method exploits the dichromatic reflection to analyze the angular period of each illumination direction, which makes it

possible to separate the reflected light for each illumination. This adaptive method acquires reflectance properties rapidly.

Finally, I show the usefulness of 8-D reflectance fields. Although few techniques have been proposed that use 8-D reflectance fields, this does not mean the applications are useless. I propose a useful application, the hemispherical confocal imaging. This technique can capture only a particular depth clearly, only when the measuring system provides 4-D illumination and observation in various directions on a hemisphere around the target.

In this research I have established the fundamental techniques for practical 8-D reflectance field imaging by designing a measuring system, rapid measurement technique, method of computation, and novel computational photography techniques.

List of Publications

A. Journal Papers (Full paper reviewed)

1. **Seiichi Tagawa**, Yasuhiro Mukaigawa, Jaewon Kim, Ramesh Raskar, Yasuyuki Matsushita, and Yasushi Yagi, "Hemispherical Confocal Imaging," IPSJ Transactions on Computer Vision and Applications, Vol.3, pp.222-235, Dec. 2011.

2. 田川 聖一, 向川 康博, 八木 康史, "複数光源の同時照明による BRDF の高速計測," 電子情報通信学会論文誌 D, Vol.J92-D No.8, pp.1393-1402, Aug. 2009.

B. International Conference (Full paper reviewed)

1. **Seiichi Tagawa**, Yasuhiro Mukaigawa, and Yasushi Yagi, "8-D Reflectance Field for Computational Photography," Proc. 21th International Conference on Pattern Recognition (ICPR2012), Nov. 2012.

2. Yasuhiro Mukaigawa, **Seiichi Tagawa**, Jaewon Kim, Ramesh Raskar, Yasuyuki Matsushita, and Yasushi Yagi, "Hemispherical Confocal Imaging using Turtleback Reflector," Proc. 10th Asian Conference on Computer Vision (ACCV2010), pp.331-344, Nov. 2010.

C. Domestic Conference (Full paper reviewed)

1. 田川 聖一, 向川 康博, 金 宰完, ラメシュ ラスカル, 松下 康之, 八木 康史, "亀甲多面鏡を用いた半球状共焦点撮影," 画像の認識・理解シンポジウム (MIRU2010), Jul. 2010.

2. 田川 聖一, 向川 康博, 八木康史, "複数光源の同時照明による BRDF の高速計測," 画像の認識・理解シンポジウム (MIRU2008), pp.745-752, Jul. 2008.

3. 向川 康博, **田川 聖一**, 八木康史, "複数光源の同時照明による反射特性の高速計測," 第 14 回 画像センシングシンポジウム SSII08, June 2008.

D. Domestic Conference (Without review)

1. **田川 聖一**, 向川 康博, 八木 康史, "多面体鏡を用いた 8 次元リフレクタンスフィールドの計測," 附置研究所間アライアンスによるナノとマクロをつなぐ 物質・デバイス・システム創製戦略プロジェクト成果報告会, Mar. 2011.

2. **田川 聖一**, 向川 康博, 松下 康之, 八木 康史, "多面体鏡を用いた 8 次元リフレクタンスフィールドの計測とコンピュテーショナルフォトグラフィへの応用," 情処研報 CVIM 174-11, Nov. 2010.

3. **田川 聖一**, 向川 康博, 八木 康史, "亀甲多面鏡を用いた半球状共焦点撮影," 附置研究所間アライアンスによるナノとマクロをつなぐ物質・デバイス・システ ム創製戦略プロジェクト キックオフミーティング, Aug. 2010.

4. **田川 聖一**, 向川 康博, 金 宰完, ラメシュ ラスカル, 松下 康之, 八木 康史, "多面体鏡を用いた仮想カメラ・プロジェクタ群による半球状共焦点撮影," 情報処理学会関西支部 ユニバーサルコミュニケーション研究会, June 2010.

5. **田川 聖一**, 向川 康博, 八木 康史, "複数光源の同時照明による BRDF 計測の高速化," 情処研報 CVIM 163-12, pp.77-84, May 2008.

Acknowledgements

Contents

Chapter 1

Introduction

People post many photos on the internet of things that fascinate us. Almost all of them use digital cameras to capture such scenes. Because recent digital cameras have megapixel resolution, a captured image can provide us with details of the target scene. However, the appearances of the scenes change with the focus, viewpoint, and lighting, which cannot be changed once the images are captured. That is because an image has just two-dimensional information.

The image represents information from the rays that reached a camera lens. When the lens gathers rays from the object focal point, the rays are refracted and converge at a sensor at the image focal point. Here, the information of every ray is collapsed into one pixel intensity, where the variation of each ray angle is lost in the captured image. In a lens, the focal plane is changed by changing the variation of the gathered ray angles. So, if we have all of the ray information for every angle, we can produce an image when focusing at an arbitrary depth.

The ray information is provided by the illumination of the scene from surrounding light sources. When the illumination varies, the ray information consisting of reflected light from the scene also varies. Hence, to store appearances of the scene, we should measure all information in every reflected illumination ray

However, it is difficult to completely measure it. In this dissertation, I address the problem.

1.1   Computational Photography

To acquire more information about a scene than just an image, we should know how information is lost in capturing an image by camera. Also, we should consider how to maintain, at least, the important information in captured rays for specific applications.

The digital camera has evolved so that we can store a beautiful scene in a vivid image with high-resolution sensors and digital image processing. However, the scheme of capturing has not changed except for replacement of sensitive films with digital sensors. Present cameras use

a conventional lens, diaphragm, and flash to capture images. Hence, because the process of maintaining information has not changed, much information has been collapsed.

Recently, many researchers have been interested in changing this scheme. In computational photography, the lens aperture has been coded to make all-in-focus images [1]. The exposure time has also been coded to deblur images that capture moving objects [2]. Although conventional cameras do not always need image processing to provide us with an image, novel cameras often need image processing to provide us with an excellent image. This way, computational photography can create great effects in an image using computation-based optics.

So far, photography has been about integrating ray intensities from a scene. The lighting is used only for flash. However, because illumination conditions change appearances, sophisticated illumination can add novel features to photography. For example, Kim et al. [3] have proposed a simple but very interesting technique. In highlighted depth-of-field photography, a projector projects aand focuses a pattern onto the target object. Here, the patterns on the other objects are blurred. Kim et al. [3] analyzed the focused pattern to brighten the target object and darken the other objects. So, they used a projector as sophisticated illumination and successfully emphasized the target object.

In brief, the purpose of computational photography is to maintain important properties of a scene in a captured image via specially designed optics. Camera optics and scene illumination have been designed to achieve this. Here, it is important to understand what property can be included in a captured image.

1.2   8-Dimensional Reflectance Field

An image captured by a camera represents an appearance of a scene under specific conditions. What we can acquire from images is determined by the limitation of the finest appearance information.

The appearances of an object or a scene depend on how the light is reflected at the surface. If we want to control the appearance freely, we need all of the properties of the scene. So, in computer graphics great effort has been made to create realistic images of synthetic objects that do not really exist. To do this, many researchers have addressed how to measure the property, how to model the property, how to image the property, and how to deal with the interreflection. However, if we want to control the appearances of real objects under arbitrary illumination, we can do it using reflectance fields of the scene. This is called an image-based technique: image-based rendering, and image-based relighting.
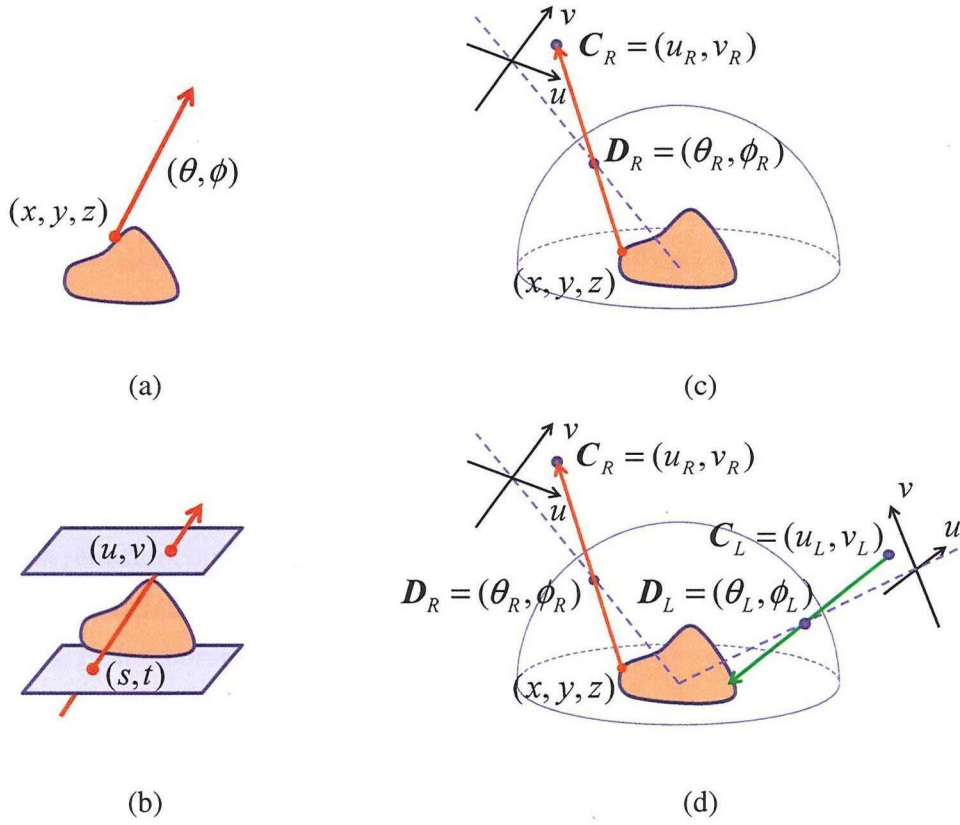
Figure 1.1: Descriptions of the light and reflectance fields. Both illumination and reflection can be described as a 4DLF. Hence the combination can be represented as an 8DRF.

The image of a scene varies when the viewpoint or the illumination changes. It is well known that an appearance can be perfectly represented by a set of rays.

First, we consider rays reflected from the scene. A ray can be expressed by the passing point (x, y, z) in the direction (θ, ϕ) as shown in Fig.1.1(a). Hence, the intensity of the ray can be defined by five parameters. This description of the rays is called the *light field*. Here, assuming the ray is not attenuated, the intensity of the ray can be defined by four parameters, (s, t) and (u, v), on two planes as shown in Fig.1.1(b). While this is a standard representation, it cannot describe rays that are parallel to the two planes. Hence, in this research we define the light field using a hemisphere that covers the scene as shown in Fig.1.1(c). The ray is denoted by its position on the hemisphere $\boldsymbol{D}_R = (\theta_R, \phi_R)$ and its direction $\boldsymbol{C}_R = (u_R, v_R)$. This is a four-dimensional light field (4DLF) denoted by $F_R(\boldsymbol{D}_R, \boldsymbol{C}_R)$, which can represent all the rays reflected from the scene.

Similarly, the illumination on the scene is also described as a light field. As shown in Fig.1.1(d), the incident ray can be defined by its position on the hemisphere $\boldsymbol{D}_L = (\theta_L, \phi_L)$

and its direction $C_L = (u_L, v_L)$. Hence, we can denote the 4DLF of the illumination by $F_L(D_L, C_L)$.

The relationship between the 4DLF of the illumination F_L and the 4DLF of the reflection F_R is called the *reflectance field*. Hence, we can denote the reflectance field with eight parameters by

$$F(D_L, C_L, D_R, C_R), \tag{1.1}$$

consisting of the two 4DLFs of illumination and reflection. This eight-dimensional reflectance field (8DRF) can perfectly describe the image of the scene from arbitrary view points under arbitrary illumination conditions.

Ultimately, using a projector and camera, we can acquire the information on rays in a 3-D scene as an 8-D reflectance field.

1.3 Computational Photography based on 8-Dimensional Reflectance Field

If the 8-D reflectance fields can be measured and computed, we can realize various applications, exploiting the information by controlling the illumination and observation.

The quality of industrial and consumer products should be assessed with appearances of high accuracy. We should understand how product appearances vary with every viewing angle under various lighting conditions. The 8-D reflectance field can completely represent the appearances. Further, to guarantee processing accuracy, the appearance information can give clues to detect product flaws. That is because even microscopic flaws and bumps on the surface of the target object reflect its appearance like a Chinese magic mirror, which looks like a planar mirror but actually has slight bumps on the surface that reflect sunlight toward a planar wall with a pattern that depends on the bumps. Hence, if the difference in appearance between products with and without flaws could be measured, a flaw could be detected and quantitatively verified.

Similarly, appearances could be stored accurately and in high detail for archiving objects of cultural heritage. If they have been measured, the appearances can be reproduced for any observation conditions and shown to people who cannot go to the places where the objects are displayed. Because the appearance depends on the reflectance properties of the target materials, we should store information on the reflectance properties by measuring the materials in detail.

However, no application techniques have been developed that use the 8-D reflectance field. So, I have developed the *measuring device* and *computing framework* for an 8DRF, and will apply it to an example.

4

1.4 Outline

I have discussed on the practical use of an 8-D reflectance field. In this dissertation, I describe how to measure and apply it. The dissertation is organized as follows.

Chapter 3 I design a mirror device to measure reflectance fields. The target reflectance fields are not restricted to 8DRFs and include lower-dimensional ones. I explain how to exploit conic curves to design mirrors and describe the difference between curved mirrors and polyhedral mirrors. Last, I show how to implement the turtleback reflector designed to measure an 8-D reflectance field uniformly and widely. For a spherical distribution, I used an ellipsoidal shape to exploit the characteristics. For uniformity, I used a geodesic dome that can be approximated as a regular polyhedron. With this, I developed a turtleback reflector consisting of fifty mirrors. Combining it with a projector and camera, each mirror makes a virtual projector and camera on a hemisphere with a uniform density. Thus, I can illuminate a target scene with fifty projectors and observe the light reflected from the scene with fifty cameras. This is the measurement of 8-D reflectance fields.

Chapter 4 I introduce a lower-dimensional slice of the 8-D reflectance field. An 8DRF includes the reflectance properties that can represent generalized appearances of materials. The representations do not always use all the dimensions of 8DRFs. With four dimensions, we can assume a type of four-dimensional reflectance field to be a bi-directional reflectance distribution function that represents reflectance properties of opaque and homogeneous materials. We can assume a type of six-dimensional reflectance field to be a bidirectional texture function that represents reflectance properties of opaque and inhomogeneous materials. If using all eight dimensions, we can assume the 8-D reflectance field to be a bi-directional scattering surface distribution function that represents reflectance properties of general translucent materials.

Chapter 5 I describe a rapid measuring technique for reflectance fields. First of all, I address the measurement of isotropic BRDFs, which consists of a three-dimensional reflectance field, for clues to physically analyzing 8-D reflectance fields. In the technique, I multiplex illumination using dichromatic reflection. However, the isotropic BRDF does not assume that the reflected light is not overlapped in every direction. So, under multiplexed illumination, the reflected light generally overlaps in some directions, and we cannot restore reflected light for every direction of illumination. Here, I show how the overlapped reflection can be restored if the illumination is multiplexed adaptively for the target reflectance property.

Chapter 6 I propose a framework for imaging 8-D reflectance fields. Because there is much information in the 8-D reflectance field, a method of image computation is needed that creates an image with novel characteristics that cannot be seen in a normal image. Also, the computational framework is useful for considering the previously proposed techniques. This shows the similarity among the techniques. To confirm the usefulness of the framework, I unify three computational photography techniques using my framework with the turtleback reflector system.

Chapter 7 I propose a novel application to image a particular depth clearly. Here, I show how to analyze 8-D reflectance fields by controlling the illumination and observation. For the illumination, I propose focused high-frequency illumination to illuminate only the desired depth with a computation of high-dimensional illumination. To reduce undesired effects in the computed image of the target depth, I analytically factorize the images into reflectance and three undesired effects consisting of occlusion, attenuation, spatially varying illuminance.

1.5   Contribution

- I designed a measuring device for 8DRFs which exploits conic curve characteristics. Hence, designing the measuring devices becomes easy.

- I established a computational framework that uniformly expresses some computational photography that relates light fields and reflectance fields. WIth this, The relationships among presented techniques become clear.

- I showed that the usefulness of measuring 8-D reflectance field on a hemisphere by proposing a novel imaging technique that clearly capture an occluded and attenuated surface texture.

- I showed that the high dimensionality is very useful by the proposed device and application even if the resolution is quite low because of a trade-off between the measuring resolution and dimension when using a mirror system like the turtleback reflector that has many planar mirrors.

Chapter 2

Related Work

2.1 Measuring Device

Reflectance Property

To represent general appearances of an object, reflectance properties of materials which the object consists of is useful. The reflectance property is dependent on the microscopic shape and the opacity of the material surface. The reflectance property can be used for various applications, for example, creating realistic computer graphics, inspections of painted surfaces, and so on. So far, various measurement systems have been developed. Li et al. [4] have developed the gonioreflectometer which is a straightforward device to measure BRDFs by rotating the sensor and light source around the target material. The systems using concave mirrors [5] [6] have developed to speed-up the measurements where the mirrors gather reflected light from a target point on the material surface. However, to measure fine reflectance properties, it takes tremendously long time because the measurement system must illuminate the target point in all directions individually, and measure the reflected light in all directions for each illumination, especially for the system with mechanical drives.

Recently, to measure fine reflectance properties rapidly, the systems combining a projector with a concave mirror. Mukaigawa et al. [7] use an ellipsoidal mirror, and Ghosh et al. [8] use an originally designed mirror. In these systems the mechanical drive to change illumination directions is replaced with the projector that changes the illumination directions by changing projected patterns rapidly. Moreover, by the concave mirror, a camera can capture all of the reflected light at once.

Reflectance Field

A light field is a 4-D slice of the 8-D reflectance field under static illumination. It can be recorded by a scanning camera [9] or installing many cameras [10]. Alternatively, a high-

resolution camera can be combined with a micro lens array [11], a micro mirror array [12], or masks [13]. To vary the illumination, Debevec et al. [14] rotated the light source, and Sen et al. [15] used a projector as the light source. Masselus et al. [16] rotated the projector, and Matusik et al. [17] rotated both the light source and the camera to measure a 6-D reflectance field. Müller et al. [18] used 151 cameras with flashes.

In principle, the complete 8-D reflectance field can be measured by installing many projectors and cameras densely on a hemisphere. However, it is difficult to realize such a system because of the cost and the physical interference between the devices. While a rotating projector and camera solves these problems, the capture process is impractically long. Recently, Garg et al. [19] and Levoy et al. [20] used multiple planar mirrors and Cossairt et al. [21] used a lens array to measure a part of the 8-D reflectance field, but the direction of the illumination and observation was limited to a narrow angle.

2.2   Rapid Measurement Method

There is an advantage of using a projector as a light source. Because the projector can generate light sources in various directions simultaneously, multiplexing techniques can be applied to illumination methods.

Multiplexed Illumination using Compression Transform

Mukaigawa et al. [22] has multiplexed the projected patterns with the Hadamard transform and improved the S/N ratio of reflectance property measurements. It has been shown that the measuring time has been reduced by orthogonal transforms of illumination distributions on the projected patterns, Ghosh et al. [8] and Sato et al. [23] used the spherical harmonics, and Peers et al. [24] used the wavelet transform. However, although the Hadamard transform can improve the S/N ratio, it cannot reduce the measuring time. On the other hand, the techniques using the spherical harmonics or the wavelet transform can reduce the measuring time but cannot measure the proper reflectance property. If such compression techniques are used, the high frequency components of the reflected light from smooth surfaces cannot be kept because the transforms restrict the measured components to the low frequency components.

Adaptively Multiplexed Illumination

Sen et al. [15] showed that the measuring time is reduced without loss when the reflected lights of multiplexed illumination are not overlapped, in confirmation of their Dual Photography technique, which exploit the Helmholtz reciprocity to interchange the lights and cameras. However,

it cannot be applied to measurements of reflectance properties because the target point is the same for every illumination and the reflected light is always overlapped.

Compressive Sensing

Recently, the compressive sensing [25] [26] [27] has been well known as a useful technique to reduce the measurement time. The technique exploits data-sparseness in target information. The data-sparseness means that the information signal can be well compressed by compression transforms like the Fourier transform, and many coefficients are zero. Here, the number of non-zero coefficient is the length of minimum signal representing the information. So, when one entry of the signal is measured at one time, the measuring time can be reduced by the compressive sensing.

For measurements of reflectance fields, Peers et al. [28] have shown that the compressive sensing can be applied to the measurement of light transport, which is a six-dimensional reflectance field consisting of two-dimensional reflection under four-dimensional illumination. They have reduced the measuring time by the compressive light transport sensing, exploiting the sparseness in the light transport matrix.

2.3   Imaging Technique on Depth of Field

Many researchers have developed photography techniques to clearly capture the scene with various DOFs which covers their targets. To shrink a DOF, they used a camera array or a lenslet array. To extend a DOF, they used coded apertures analyzed in the frequency domain.

Shallowed Depth of Field

The synthetic aperture imaging virtually create a larger aperture having a shallow DOF. Also the imaging technique can change the depth of the focal plane after capturing the scene, well-known as the refocusing technique. Vaish et al. [10] developed a dense camera array to do it. Ng et al. [29] developed a hand-held plenoptic camera within a lenslet array. Recently, a light field camera is commercially available. Levin et al. [30] develop the lattice-focal lens consisting of parts of different focal lenses to keep high frequency information in the wider DOF than the DOF of each single lens.

Extended Depth of Field

Often, a DOF of a SLR camera is too shallow to capture whole a region of interest in a target scene. So, researchers have developed methods extending a DOF using coded apertures. The coded aperture can convolve a coded PSF into a captured image. This can leave the high frequency component of the captured scene in the captured image. Therefore, an image clearly focused on whole the scene can be restored.

Aesthetic Imaging Techniques

There are many imaging techniques exploiting bokeh as an aesthetic effect. By controlling bokeh, impressive effect is given to photos. Lanman et al. [31] analyzed the spatially-varying point spread function to control bokeh. Kusumoto et al. [32] controlled defocus in the synthetic aperture imaging by an image interpolation of uncalibrated multiview images.

2.4 Imaging Technique for Object in Scattering Media

Incident light upon murky liquids or translucent media scatters, and the appearance becomes blurred. To obtain clear views, descattering methods have been developed. Treibitz and Schechner [33] used a polarizer under water. Kim et al. [34] used a lenslet array. Assuming that only single scattering is observed in optically thin media, Narasimhan et al. [35] estimated a 3-D shape with descattering and Gu et al. [36] estimated the 3-D distribution of inhomogeneous scattering media.

Recently, Fuchs et al. [37] combined confocal imaging with descattering, which captured a descattered image at a particular depth in a 3-D scene. This technique consisted of the synthetic aperture confocal imaging proposed by Levoy et al. [20] and the high frequency illumination proposed by Nayar et al. [38]. While our method is based on this idea, we combine a factorization method to remove the effect of any attenuation remaining in the descattered images.

Chapter 3

Measuring Device for 8-D Reflectance Field

To measure 8DRFs, a target scene needed to be illuminated in every direction at every point on a hemisphere. Similarly all the reflected light needed to be measured.

To generate illumination in various directions passing through a point on a hemisphere, we can use a projector, that can be considered as a generator of two-dimensional light fields. If many projectors are densely placed on a hemisphere, the total system can be considered as a generator of four-dimensional light fields. On the other hand, a camera can capture the rays passing through the center point of the camera in various directions. Thus, a camera can be considered as a measurement device of two-dimensional light field. If many cameras are densely placed on a hemisphere, the total camera system can be considered as a measurement device of four-dimensional light field. Therefore, to develop a system that can measure 8DRFs is to place many projectors and cameras on a hemisphere densely.

3.1   Problems on Measurement

3.1.1   How to Sample 8-D Reflectance Field

The most simple way to measure 8-D reflectance fields is to move a projector and camera on a hemisphere, capturing a target scene illuminated by the projector with all possible patterns. Of course, it is unrealistic for some reasons. First, a 8-D Reflectance Field will be a tremendously large data because of the high dimensionality. Second, such a measurement takes extremely large time costs. So, because it is infeasible that a whole 8-D reflectance field cannot be completely measured, we have to adequately sample it, where all the dimensions are treated uniformly.

3.1.2 How to Locate Optical Devices

Another problem is how to decide the way to locate projectors and cameras. Simply, the projectors and cameras can placed on a hemisphere if the distribution can be sparse. However, if the distribution of projectors and cameras must be dense, it is difficult to place them on a hemisphere because of the physical conflicts of the bodies.

3.2 Mirror Systems to Measure Reflectance Field

A mirror can translate a point passed through by a ray to the mirrored point. Hence, developing a measurement system can be considered as placement of mirrors in order to make the mirrored point at an arbitrary position on a hemisphere. Using mirrors, development of a measuring system becomes easier because arranging many mirrors is easier than arranging many projectors and cameras.

3.2.1 Mirror Device Designs via Property of Conic Curves

Conic curves are well known as curvatures with focal points. For a curved line with focal points, a mirror along the line gathers rays at the focal point. Conic curves can be classified into four types: circle, ellipse, parabola, and hyperbola. Here, the target scene is three-dimensional, not two-dimensional. So, a three-dimensional curved surfaces are needed and they are a sphere, ellipsoid, paraboloid, and hyperboloid, respectively. Here, for simplicity, I describe about the lines not the surfaces and about arrangements of cameras. Note that designs for cameras can be applied to arrangements of projectors in the same way. In this section, I explain how to use the conic curves to arrange mirrored points on a hemisphere.

When mirrors are arranged along a circle, we can exploit characteristics of the circle, where rays passing through the center are reflected at the curve and passes through the center again. Here, the total path length is always twice of the radius. So, the mirrored point is created on a circle with twice radius. To exploit this, a camera and a target scene are needed to be placed at the center of circle. It is physically impossible. However, it is possible optically using beam splitters can be used as shown in Fig. 3.1(a).

When mirrors are arranged along an ellipse, the ray passing through one focal plane is reflected on the mirror and reach the other focal point. Here, the total path lengths are always constant. Hence, placing a camera at one focal point and a target scene at the other focal point, a virtual camera is created on a circle, as shown in Fig. 3.1(b).

When mirrors are arranged along a parabola, characteristics of a parabola can be exploited. Distances from a point on a parabola between to a directrix and a focal point is always the same. Therefore, when a camera is placed along the directrix, a virtual camera is placed on a circle that has the center at the focal point of the parabola, as shown in Fig. 3.1(c).

When mirrors are arranged along a hyperbola, characteristics of hyperbola can be exploited as shown in Fig. 3.1(d). In a hyperbola, there are two focal points and two curved line, a differential length between from two focal points to a point on a line is always constant. Here, a ray going to one focal point is reflected at the curved line α and goes to the other focal point. Hence, in order to let a target scene be placed at one focal point, where mirrored points created on a circle, surrounding the scene, the incident points are needed to be placed on a circle centered at the other focal point. So, the hyperbola cannot be used because such a setting assumes the purpose condition is already satisfied, where a point is surrounded by points on a circle.

3.3 Ellipsoidal Mirror to Measure Dense 4-D Reflectance Field

Using a conically curved mirror, we can let illuminating rays from a projector and viewing rays of a camera at a focal point be focused at the other focal point. When we need high resolution for angular variation to the target point, the curved mirror can help to measure such a reflectance property. An advantage of this kind of mirrors is the ability to transform central projection into converging projection. This way, pixels of a projector and camera which look at different points can look at the same point in various directions.

Mukaigawa et al. [7] [22] have developed a measuring system named RCG2 with an ellipsoidal mirror, as shown in Fig. 3.2(a), to rapidly and finely measure BRDFs. As shown in Fig. 3.2(b), using a beam splitter, a projector and camera are placed at the same focal point of an ellipsoid. So, in this system, a target point on a surface of target materials can be illuminated and observed in various directions at the same time by change of projected patterns.

3.4 Turtleback Reflector to Measure 8-D Reflectance Field

3.4.1 Polyhedral Mirror

To generate and capture 4-D light fields for a 3-D scene, projectors and cameras should be placed uniformly on a hemisphere. Here, the curved mirror cannot be used because they focus all rays at a single point though the target scene is not a point but a space.

To realize this, we used planar mirrors. By combining a projector and camera with many planar mirrors, a number of virtual projectors and cameras with low resolution can be generated and can capture the scene in various directions.

Views from the virtual cameras are created in a view from the real camera. Hence, the region for each virtual camera must be cropped and warped to get virtual viewpoint images. Geometric calibration of the virtual cameras is performed by finding corresponding points in a captured image using the real camera. The geometric conversion from the real camera to virtual cameras can be achieved using simple homography. The pixel intensities of the virtual image are resampled from the captured image.

3.4.2 Adaptive Curves for Polyhedral Mirror

To measure 8DRFs, the planar mirrors should be properly positioned, so that they place virtual cameras on a hemisphere. A distance between the target and each virtual camera should be constant. To do this, as mentioned above, conic curves can be exploited. Practically, the designs by an ellipse and a parabola are useful. These designs are suitable for different projection systems.

For a perspective projection, the planar mirrors should be located along an ellipsoid as shown in Figure 3.1(b). On the other hand, if the projection is orthographic, the planar mirrors should be located along a paraboloid as shown in Figure 3.1(c).

In the design using a paraboloid, a telecentric lens is needed. However, the telecentric lens is expensive. Hence, we adopted the design using an ellipsoid because it just requires a conventional lens.

3.4.3 Polyhedral Mirror Design for Uniform Sampling

In practice, the number of virtual cameras is finite. Cameras are discretely placed on a hemisphere. To measure 8DRFs, the virtual cameras should be placed with as uniform a density as possible.

As shown in Figure 3.3(a), a geodesic dome is a well-known polyhedron that uniformly samples a sphere. The virtual cameras are located on the facets of the geodesic dome. The hemispherical aperture is then divided by the facets as uniformly as possible. The mirrors are located on tangent planes on the ellipsoid. The tangent point is given by the projection of the center of the facet from the center of the dome. To decide the mirror shape, the vertices of the facet are projected on to the tangent plane. These mirrors become the polyhedral mirrors, which place virtual cameras on a hemisphere with uniform density.

Each facet of the polyhedron acts as a viewing window corresponding to the virtual camera. A region commonly observed from all virtual cameras is defined by a logical AND of all the views of the virtual camera. That is, the shape of a facet should be close to a circle in order to observe a large area. Therefore, we used the dual geodesic dome shown in Figure 3.3(b) instead of the original geodesic dome, because the dual dome has pentagonal and hexagonal facets, while the original geodesic dome had triangular facets.

3.4.4 Implementation of the Turtleback Reflector

We now show an implementation of our polyhedral mirror. We first decided on the number of mirrors. The geodesic dome is made by dividing 20 facets of an icosahedron into $20 \times 4^k (k \in \mathbf{N})$ facets. The number of facets of the dual dome is then $N = 10 \times 4^k + 2$. We set $k = 2$ and $N = 162$. The upper half hemisphere consists of 81 facets. However, 81 facets do not completely cover the upper hemisphere. Hence we added 10 horizontal facets, which are located at the border of the upper and lower hemispheres. In total we used 91 facets.

In the design shown in Figure 3.1(a), the target object occludes some mirrors. Hence, we combined two ellipsoids as shown in Figure 3.4. In this design, the two polyhedral mirrors place the virtual cameras over the whole surface of the hemisphere.

We designed one polyhedral mirror because pairs of polyhedral mirrors are symmetrical. To fix the mirror patches, we designed a frame as shown in Figure 3.5. This frame is made by stereolithography and planar mirror patches are attached to the frame. Fifty mirror patches completely cover half of the hemisphere. The frame with mirror patches is the *turtleback reflector* as shown in Figure 3.6.

3.4.5 Total optical device

In this research, we combine the turtleback reflector with a coaxial pairing of a high-resolution camera (PointGrey, Grass-50S5C, 2448 × 2048) and a small projector (KAIREN Projector X Pro920, 640 × 480) using a beam splitter as shown in Figure 3.7.

The device is designed to measure a small area of 6 × 6 mm. By resampling the captured image using a real camera, images of the virtual cameras whose resolution is 60 × 60 pixels are generated. For a virtual projector, we resample the target area using a 20 × 20 format. Hence, the resolution of the virtual projector corresponds to 20 × 20 pixels.

Theoretically, both the illumination and observation can be focused only on a particular depth in the scene and the DOF becomes zero. However, we implemented only half of the whole turtleback reflector. Therefore, strictly the DOF of our prototype system is not zero but shallow.

(a) Sphere

(b) Ellipsoid

(c) Paraboloid

(d) Hyperboloid
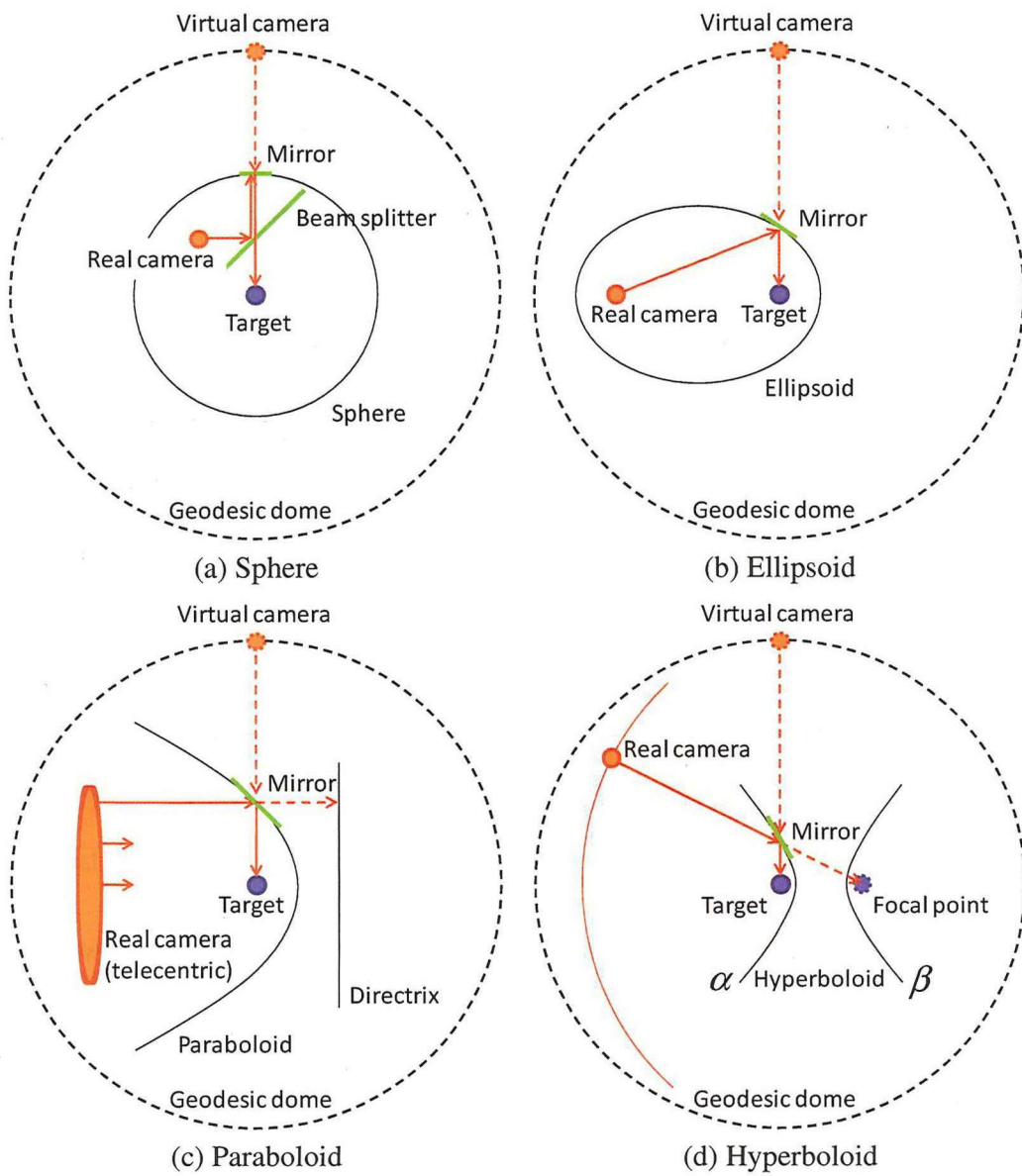
Figure 3.1: Design of mirrors using conic curved surfaces.
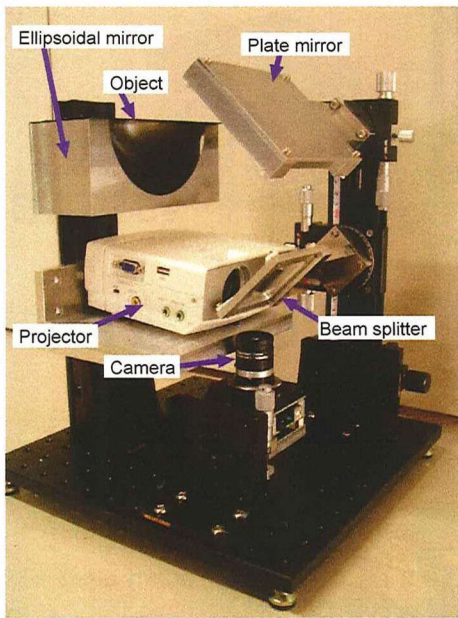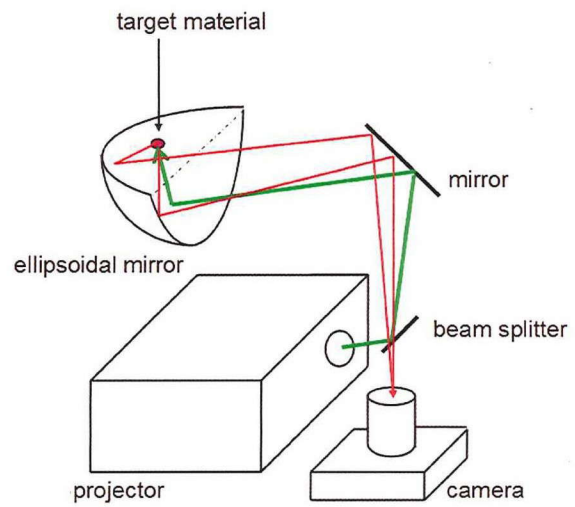
(a)Overview   (b)Path of ray

Figure 3.2: BRDF measuring device. [22]

(a) A geodesic dome   (b) The dual

Figure 3.3: Geodesic domes.
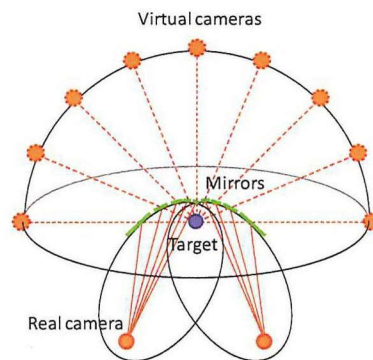
Figure 3.4: Design of polyhedral mirrors using two ellipsoids.

(a) front view   (b) bottom view   (c) dimensions
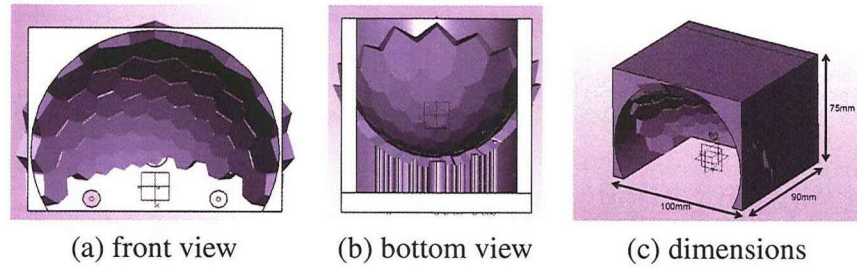
Figure 3.5: Design of the frame for the turtleback reflector.

Figure 3.6: Turtleback reflector.
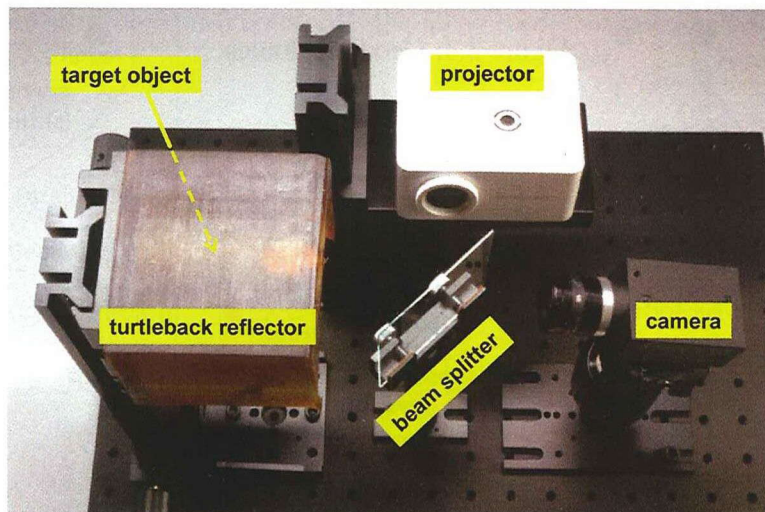
Figure 3.7: Total optical device for hemispherical confocal imaging.

18

Chapter 4

Slices of 8-D Reflectance Field

4.1 Overview of Low-Dimensional Slices

8DRFs have much information on a scene. So, appropriate slices represent useful functions (Table.7.1). To represent reflectance properties, all the dimensions are not always needed. Here, I describe three reflectance properties as slices of an 8DRF. First, I show a slice that can represent reflectance of a opaque material. Next, I show a slice that can represent reflectance of a texture. Finally, I show a slice that can represent reflectance of a translucent object.

Table 4.1: Low dimensional slices and Applications.

	Representations with 8DRF
BRDF	$BRDF(\boldsymbol{D}_L, \boldsymbol{D}_R) = F(\boldsymbol{D}_L, (0,0), \boldsymbol{D}_R, (0,0))$
BTF	$BTF(\boldsymbol{D}_L, \boldsymbol{S}, \boldsymbol{D}_R) = F(\boldsymbol{D}_L, P_L(\boldsymbol{D}_L, \boldsymbol{S}), \boldsymbol{D}_R, P_R(\boldsymbol{D}_R, \boldsymbol{S}))$
BSSRDF	$BSSRDF(\boldsymbol{D}_L, \boldsymbol{S}_L, \boldsymbol{D}_R, \boldsymbol{S}_R) = F(\boldsymbol{D}_L, P_L(\boldsymbol{D}_L, \boldsymbol{S}_L), \boldsymbol{D}_R, P_R(\boldsymbol{D}_R, \boldsymbol{S}_R))$

4.2 Bidirectional Reflectance Distribution Function

For opaque objects with uniform reflectance property, the property of only one point on the surface can represent the reflectance properties for all points of whole surface. It is the Bidirectional Reflectance Distribution Function (denoted as BRDF in the following).

In the BRDF, the observed point is only one. So, it can be the center $(0,0)$ of the hemisphere. When the target point is illuminated in the direction $\boldsymbol{D}_L$, the reflected light in the direction $\boldsymbol{D}_R$ can be represented in BRDF as

$$BRDF(\boldsymbol{D}_L, \boldsymbol{D}_R) = F(\boldsymbol{D}_L, (0,0), \boldsymbol{D}_R, (0,0)). \qquad (4.1)$$

Thus, we can see that the BRDF is the four-dimensional slice of the 8DRF as shown in Fig. 4.1.

19

Figure 4.1: BRDF.

4.3 Bidirectional Texture Function

For opaque objects with partially varying reflectance properties, on the surface, the points to be measured are all the surface points of the objects. It is the Bidirectional Texture Function (denoted as BTF in the following).

The difference between the BTF and BRDF is the number of target points. In the BTF, the target points are not the only one. For the point at $S = (x, y, z)$ on the object surface, when only the point S is illuminated, the reflected light is measured only in the directions passing S. Thus, denoting the illumination and reflection direction as projective transformations, $P_L(D_L, S)$ and $P_R(D_R, S)$, respectively, the intensity of reflected light in the BTF is represented as

$$BTF(D_L, S, D_R) = F(D_L, P_L(D_L, S), D_R, P_R(D_R, S)). \tag{4.2}$$

In this way, we can see that the BTF is the six-dimensional slice of an 8DRF as shown in Fig. 4.2.

4.4 Bidirectional Scattering Surface Distribution Function

For translucent objects, the incident light at the surface spreads to the inside of the objects and the reflected light observed not only the incident point but other points. This inside scattering is called as the subsurface scattering, and represented by Bidirectional Scattering Surface Reflectance Distribution Function (denoted as BSSRDF in the following).

In this section, the illuminated and observed points are denoted as $S_L = (x_L, y_L, z_L)$ and $S_R = (x_R, y_R, z_R)$, respectively. The direction of rays passing through a point D_L on the

20

Figure 4.2: BTF.

Figure 4.3: Representation of a BSSRDF.

hemisphere and illuminating the point S_L can be represented by $C_L = P_L(D_L, S_L)$ using a projective transformation P_L. Thus, the intensity in the BSSRDF can be represented using the incident direction D_L, incident point S_L, observed point S_L, and outgoing direction D_R as

$$BSSRDF(D_L, S_L, D_R, S_R) = F(D_L, P_L(D_L, S_L), D_R, P_R(D_R, S_R)). \qquad (4.3)$$

So, the BSSRDF is another representation of the 8DRF as shown in Fig. 4.3.

Chapter 5

Multiplexed Illumination for Rapid BRDF Measurement

Measuring a high-dimensional reflectance field is hard because of large variation of illumination. So, I addressed measuring a low-dimensional reflectance field because the complexity is less than that of an 8DRF though the variation is still large. Here, I measure the most simple reflectance property, a BRDF because its target is a single point, which can be more easily analyzed.

5.1 Introduction

5.1.1 Isotropic and Anisotropic BRDFs

As explained in Sec. 4.2, BRDFs can represent reflectance of a material surface. A BRDF (Bi-directional Reflectance Distribution Function) is a function that returns the reflectance ratio between an illumination intensity in a direction, (θ_i, ϕ_i), and a reflection intensity in a direction, (θ_r, ϕ_r), as shown in Fig. 5.1.

There are two kinds of BRDF. One is an isotropic BRDF, and the other is an anisotropic BRDF. A reflectance property can be represented as an isotropic BRDF if observed reflectance ratio is not changed when the target surface is rotated around normal at the measured point, keeping the normal direction and incident angles of illumination and observation. If the ratio is changed, the reflectance needed to be represented as an anisotropic BRDF. An anisotropic reflection is a relatively special property as seen in hairline finished metal, fabrics, and so on. So, to represent an anisotropic reflection, four angle parameters $(\theta_i, \phi_i, \theta_r, \phi_r)$ are needed. On the other hand an isotropic reflection can be represented by three parameters $(\theta_i, \theta_r, \phi)$ because the reflectance ratio is only dependent on the relative angle between the angles ϕ_i and ϕ_r; $\phi = \phi_r - \phi_i$, for the angle of ϕ.
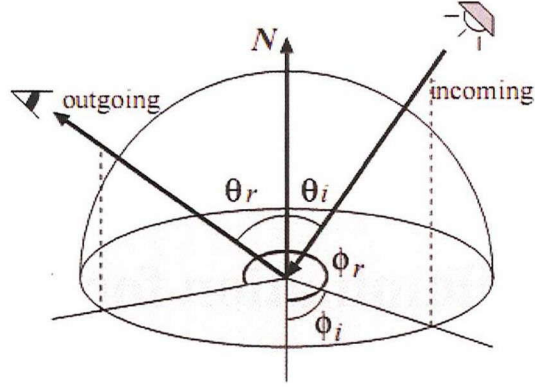
Figure 5.1: Angle parameters of BRDF.
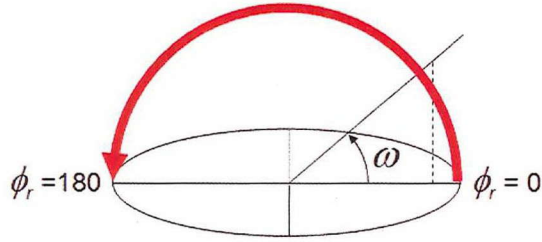
Figure 5.2: Coordinate system of illumination.

5.1.2 Measurement of Isotropic BRDF

Assuming that the reflectance property of the target object is isotropic, the RCG2, introduced in Section 3.3, can completely measure the reflectance property. In the measurement, the incident direction is changed from $(\phi = 0, \theta = 90)$ to $(\phi = 180, \theta = 90)$, passing through the normal direction $\theta = 0$, on a hemisphere, as shown in Fig. 5.2. In this chapter, the angle between the incident direction and $(\phi = 0, \theta = 90)$ is simply denoted as ω, where ω is changed from 0 to 180 to measure an isotropic BRDF. Thus, when the isotropic BRDF is sampled by one degree, the incident direction will be changed 181 times for the measurement and the reflected light will be captured.

24
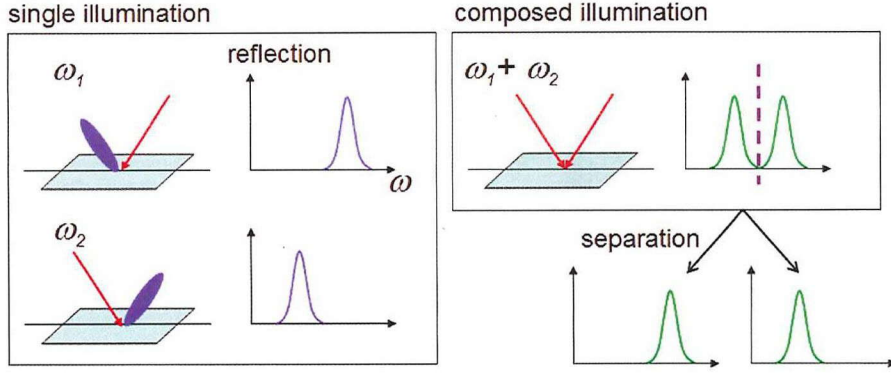
Figure 5.3: Principle of rapid measurement.

5.2 Multiplexed Illumination for Rapid Measurements

5.2.1 Principle

In this research, the purpose is reduction of total measuring time for an isotropic BRDF in which an angular interval is set to one degree. For example, as shown in Fig. 5.3, if the distributions of the reflected light for two incident directions ω_1 and ω_2 are not overlapped, when the target point is illuminated from the two directions, the reflected light under each illumination can be acquired separately. That means that the reflected light under multiplexed illumination can be separated into a set of reflected light distributions for each incident direction.

Denoting the set of multiplexed incident directions as Ω and the i-th direction as $\omega_i \in \Omega$, the problem is considered as how to restore the reflected light distribution r_{ω_i} under illumination in the direction ω_i from the total distribution r_Ω under multiplexed illumination in the directions Ω as the following equation.

$$r_\Omega = r_{\omega_1} + r_{\omega_2} + \cdots + r_{\omega_n} \tag{5.1}$$

If n incident directions can be multiplexed, the measuring time becomes $1/n$. Thus, the multiplexed measurement of the isotropic BRDF is the n times faster than the simple measurement.

5.2.2 Reflection Decomposition into Diffuse and Specular Components

In actual, distributions of reflected light overlap if the target point is illuminated simply in some directions at the same time. In this method, at first, I separate reflected light into diffuse and specular components. Second, I restore distributions of reflected light for the components individually, based on different tendencies of the components in reflected light distributions.

25
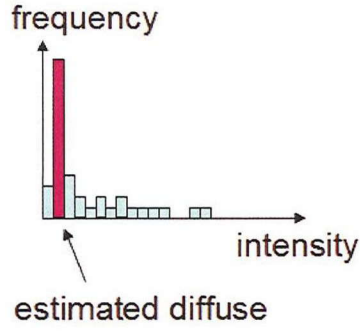
Figure 5.4: Histogram of intensities.

According to a model of dichromatic reflection, reflected light can be represented as a combination of diffuse and specular components. The diffuse reflection component can be uniformly observed in every direction. On the other hand, The distribution of specular reflection component is concentrated to a particular direction; the regular reflection direction in many cases. Because intensities of diffuse reflection are constant in every direction, the minimum value among the values measured in all directions indicates the diffuse component theoretically. However, for the system used in this research, outlier values may be measured because of the insufficient accuracy of the mirror surface finishing and noises. In the case, unfortunately, the outlier with a low value may be detected as the diffuse component.

Here, because the diffuse reflection component is observed in every direction. a mode value can be assumed to be the diffuse component. So, in the histogram of all the intensities of reflected light, the diffuse component value stand out as shown in Fig. 5.4. Once the diffuse component is acquired, the specular component can be easily acquired as a difference between the reflected light and the diffuse component.

Denoting the diffuse reflection component as d_Ω and the specular reflection component as s_Ω, its formula of decomposing the total reflected light r_Ω can be represented as

$$r_\Omega = d_\Omega + s_\Omega. \tag{5.2}$$

Although it is difficult for a general scene to decomposes the reflected light into the diffuse and specular components, in this research, it is relatively easy because the RCG2 can capture reflected light all over a hemisphere at the same time and can exploit the uniformity of diffuse reflection.

26
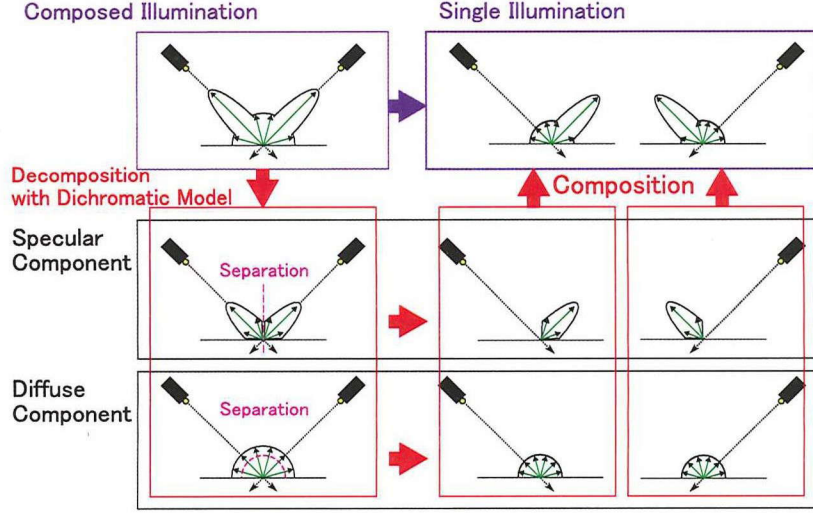
Figure 5.5: Restoration of reflected light under single illumination.

5.2.3 Restoration of Reflected Light for Single Illumination

Multiplexed diffuse and specular reflection components are individually separated for each incident direction as shown in Fig. 5.5. Thus, unlike Eq. 5.1 where the total reflected light for each incident direction is restored directly, the diffuse and specular components for each incident direction are individually restored as

$$d_\Omega = d_{\omega_1} + d_{\omega_2} + \cdots + d_{\omega_n}, \qquad (5.3)$$

$$s_\Omega = s_{\omega_1} + s_{\omega_2} + \cdots + s_{\omega_n}. \qquad (5.4)$$

Once both the components are restored, the total reflected light distribution r_{ω_i} for each incident direction can be easily restored by combinations of them as

$$r_{\omega_i} = d_{\omega_i} + s_{\omega_i}. \qquad (5.5)$$

In the following, I explain the details of restoration methods for diffuse and specular components.

Restoration of Diffuse Component

As mentioned before, diffuse reflection is uniformly distributed in every direction. Here, the intensity is proportional to illuminance on an illulminated surface. If it can be assumed that radiances of light sources are constant, illuminance from a light source in a direction ω_i is proportional to $\sin \omega_i$. Therefore, diffuse reflection for each incident direction can be restored

by an operation where the total intensities of diffuse reflection are distributed to every intensity of i-th direction in proportion to $\sin \omega_i$.

$$d_{\omega_i} = \frac{\sin \omega_i}{\sum_k \sin \omega_k} d_\Omega \qquad (5.6)$$

Restoration of Specular Component

Specular reflection is locally distributed around a direction of regular reflection. So, the distribution of specular reflection under multiplexed illumination has peak intensities in the regular directions. Also, the number of peaks equals to the number of the incident directions in the multiplexed illumination. Although, for the incident direction ω_i, the direction of the regular reflection can be simply estimated as $180 - \omega_i$, the direction of the distribution peak may be shifted by the effect of the off-specular reflection. Here, I estimate the nearest peak direction to the regular reflection direction, as the regular reflection direction correspondent to the incident direction. To separate the multiplexed distribution of specular reflection, the valleys between the peaks are found as separation directions. Searching an optimal separation direction between two adjacent peak directions can be considered as a problem of the two-class analysis. So, the discriminant analysis method can be applied, where the within-class variance is maximized and the between-class variance is minimized to find a optimal threshold. The thresholds for every two-adjacent peak directions can be estimated and the distribution of specular reflection around the regular reflection can be classified to the appropriate peak direction class. In this way, each distribution of specular reflection s_{ω_i} can be restored for the corresponding single incident direction.

5.2.4   Decision of Angular Period for Multiplexing

The restoration technique successfully separates the distribution of reflected light only when the distributions of specular reflection for each incident direction do not overlap. If the number of multiplexed incident directions increases, the measuring time can be reduced but each reflection distribution for single illumination cannot be successfully restored because of overlapping distributions. To the contrary, if the number of the multiplexed directions decreases, the distribution for each illumination can be successfully restored but the measuring time is not reduced very much. In general, for smooth surface object, more incident directions can be multiplexed because the specular reflection is more concentrated to the regular reflection direction. Thus, the optimal number of multiplexed incident direction is dependent on the target objects.

Here, the number of multiplexed directions is determined by an angular range of specular reflection under illumination from the given direction ω. For illumination from a known single incident direction ω, the diffuse and specular reflection components can be easily decomposed by the method explained in Sec. 5.2.2. The direction of the specular peak is $180 - \omega$. The range of the specular reflection determines the number of the multiplexing. Theoretically, the range can be easily estimated because the intensities of the specular reflection become to zero in the area without specular reflection. However, actually, the intensities do not become zero and the border is uncertain. Thus, I empirically set a threshold of the border intensity to $1/10$ of the peak intensity. Because there are non-zero intensities in the range determined by the threshold, the range is enlarged to the double [1]. The range is used to determine the border in the following.

Denoting the range where specular reflection can be seen as ψ, the number of multiplexed incident directions is determined as

$$n = \lceil 181/\psi \rceil. \tag{5.7}$$

In the measurements, the number of illuminating and capturing is ψ. Here, the set Ω_k of incident directions for the k-th illumination can be selected as

$$\Omega_k = \{\omega_1^k, \omega_2^k, \ldots, \omega_n^k\}, \tag{5.8}$$

where each direction is derived as

$$\omega_i^k = (i - 1)\psi + k - 1. \tag{5.9}$$

Likewise, the sets of multiplexed incident directions for each measurement can be derived: $\Omega_1, \Omega_2, \ldots, \Omega_\psi$.

5.2.5 Limitation

In the previous sections, I described the principle to rapidly measure the BRDF by multiplexing illumination. However, there are some limitations and the target is not arbitrary. In this section, I clarify the limitations of the rapid measurement technique.

In the proposed method, it is assumed that the reflected light can be decomposed into diffuse and specular reflection components. Moreover, the diffuse reflection is assumed to be modeled by Lambertian reflection model where the measured intensities of diffuse reflection are constant

---

[1] In a normal distribution, about 68 percent values are within one standard deviation and about 95 percent values are within two standard deviations. Hence, I enlarge the range to the double, to cover most of the specular reflection distribution.

29

Figure 5.6: Target object(Coin).

in all the directions. For the specular reflection, the reflection distribution must be concentrated to the regular reflection direction and not have two or more peaks. Also, when the distribution of specular reflection is widely spread, the technique cannot multiplex the illumination so much. Even if the distribution covers over 90°, the technique cannot multiplex any illumination.

The proposed method is suitable for measurements of glossy objects like smooth metal that have sharp specular reflection. On the other hand, it is unsuitable for measurements of objects like reflexive reflectors that have irregular reflectance property, where the reflection distribution has a peak in other direction than the regular reflection direction and many peaks in various directions because of the micro bump on the target surface.

Ultimately, I described the principle of the rapid measurement method for isotropic BRDFs. I have to measure four-parameter BRDF if an anisotropic reflectance property is needed to be measured. The proposed method can be applied to the measurement of anisotropic BRDFs if the previously mentioned conditions are satisfied. In the four-parameter BRDF measurements, the illumination directions are defined on a hemisphere. If the peak and distribution range of specular reflection could be estimated for directions θ and ϕ, illumination can be multiplexed theoretically. However, how to efficiently select multiplexed incident directions is a future work

5.3 Experiment

5.3.1 Evaluation of Measurement Time

To evaluate effectiveness of measuring time reduction by the proposed method, I measured an isotropic BRDF of a glossy coin as shown in Fig. 5.3.1, using the measuring device [22] introduced in Sec. 3.3. Here, the angular interval of measurements is set to one degree.

At first, to determine the number of multiplexed incident directions, an angular range of specular reflection distribution of the target object was measured. I illuminated the target in
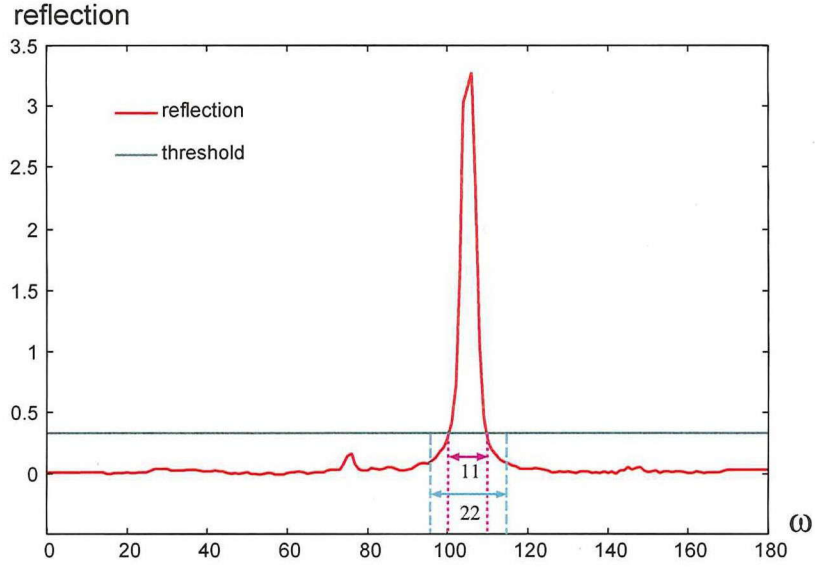
Figure 5.7: Decision of light direction interval.

the direction $\omega = 75$, and analyzed the distribution range, shown in Fig. 5.3.1 of the reflected light and estimated that the range with intensities over $1/10$ of the peak value is 11 degrees and the distributed range ψ is 22 degrees. It is confirmed that most of the specular reflection distribution is covered by this range in Fig. 5.3.1.

Thus, I acquired 9 as an optimal number of multiplexed illumination and make sets of incident directions. The first set is $\Omega_1 = \{0, 22, 44, 66, 88, 110, 132, 154, 176\}$. The reflection distribution under the multiplexed illumination is shown with red line in Fig. 5.3.1. In the distribution, sharp specular reflection can be observed separately and that of diffuse reflection is quite weak because of the smoothness of the target surface. Although the number of multiplexing is nine, only seven peaks can be seen. The distributions of reflected light are lost for illumination in the directions $\omega = 0, 176$, because the measuring device cannot measure reflectance properties in the directions of $\omega < 10$ and $170 < \omega$ owing to the insufficient accuracy of mirror surface finishing.

Next, I decompose the reflected light into the diffuse and specular components. A histogram of the measured intensities is shown in Fig. 5.3.1. In the histogram, a peak value lies in a very low intensity. Here, it was confirmed that the diffuse reflection of this coin was quite weak. For red, green, and blue components in the captured image, I made histograms of diffuse components for color components and of corresponding specular components. The diffuse and specular component histograms are shown in Fig. 5.3.1, with a blue and green line, respec-

31
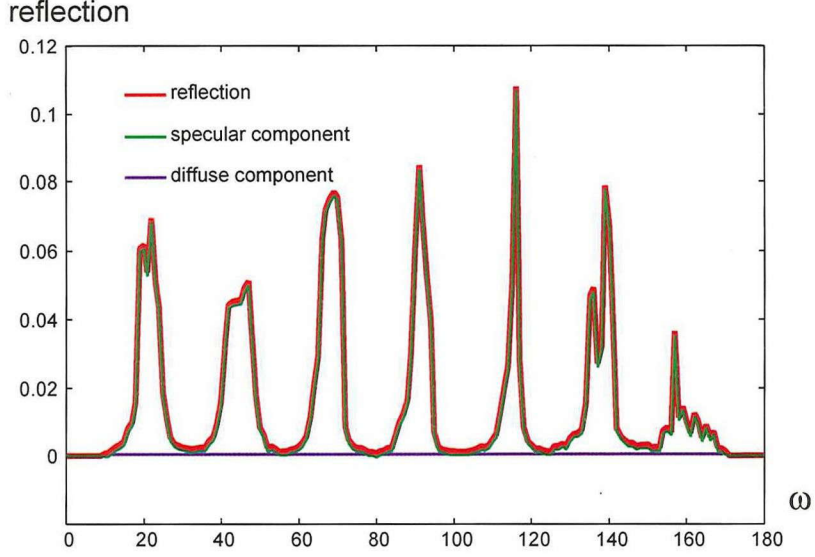
reflection

Figure 5.8: Separation of diffuse and specular reflections.

tively. In this results, it can be confirmed that the valleys between every two adjacent specular distributions are close to zero and there is almost no diffuse reflection.

Finally, I restored distributions of every total reflection for single illumination from the multiplexed distributions of diffuse and specular components, as shown in Fig. 5.3.1. In the result, it can be confirmed that the multiplexed distribution of the reflected light is successfully separated into single-illumination distributions.

To evaluate the restored distribution, I compared the result distributions with the reference distributions measured under single illumination. The result is shown in Fig. 5.3.1 where the green line indicates the reference and the red line indicates the restored. Except for the distribution correspondent to inaccessible directions $\omega = 0, 176$, the restored directions almost coincide with the reference distributions. By the result, I confirmed that the reflection distributions of single illumination could be restored from the distribution of multiplexed illumination.

To measure an isotropic BRDF with one-degree precision, it takes 181 measurement times. In the proposed method, to do this, it takes 22 measurement times. Thus, the multiplexed measurement is about 8.2 times faster than the simple measurement, theoretically. However, because there are additional tasks to remove the black level of the projected light, the total measuring time is 382 seconds and 50 seconds for simple and multiplexed measurements, respectively. Therefore, the multiplexed measurement is about 7.6 times faster than the simple measurement, actually.

32

Figure 5.9: Histogram of measured intensities.

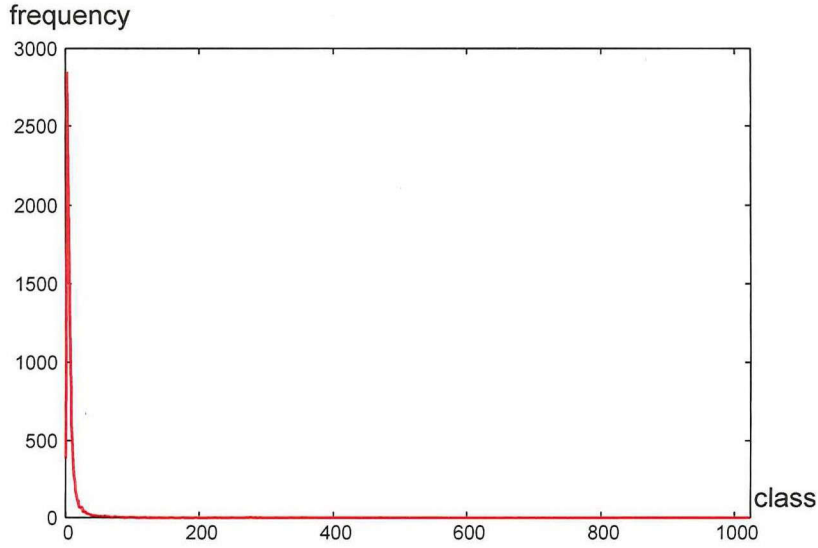## 5.3.2 Evaluation of Restored Reflection Components

In the previous section, I evaluated the restored distributions of multiplexed illumination, comparing with the reference distributions. In Figure 5.3.1, it can be seen that the diffuse components seems to be better in the restored distributions than in the reference.

To evaluate this visually, I rendered CGs of a dragon shape using measured BRDFs. Figure 5.3.1 and Fig.5.3.1 show the CGs using BRDFs by simple and multiplexed methods, respectively. In this result, for the BRDF of simple method, the red noise can be also seen in the dark region of the dragon shape. The diffuse reflection of this metal is quite weak, so the noise can significantly affect the measured intensities. However, in the multiplexed measurement, the diffuse reflection is accumulated for nine incident illuminations. So, the noise for each illumination is reduced because the total intensities of diffuse reflection is larger while the noise intensities is not changed. In Figure 5.3.1 of the multiplexed measurement result, there is no red diffuse reflection. On the other hand, in Fig. 5.3.1 of the simple measurement result, there is red diffuse reflection. In the photo of the target object as shown in Fig. 5.3.1, there is also no red diffuse reflection. Hence, the distribution out of the specular region, that creating red reflection, is considered as a noise.

To investigate the noise in detail, I measured the reflectance property by simple method 100 times and acquired the reliable reference BRDF, where the noise is averaged and disappears in many measurement times. Figure 5.3.2 shows the BRDFs by the 100-times-measuring simple method, one-time-measuring simple method, and multiplexing method with blue, green, red

33
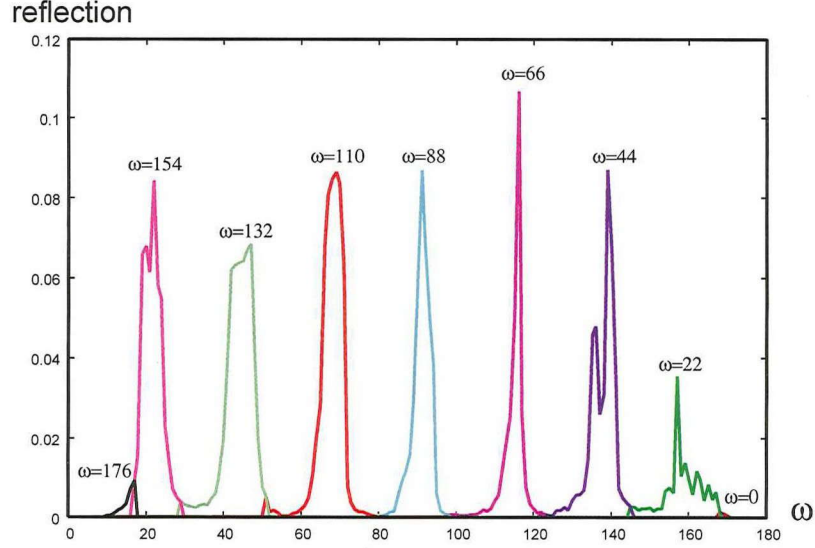
reflection

Figure 5.10: Restored reflected lights.

Table 5.1: Comparison in PSNR[dB].

Incident direction \ Illumination	single			multiplexed		
	Y	Cb	Cr	Y	Cb	Cr
45	40.80	42.86	40.35	42.38	51.89	48.04
90	40.05	42.50	37.37	38.33	49.95	40.60
135	42.99	42.04	40.77	41.02	54.37	48.35

lines, respectively. The Figure 5.3.2(a),(b),(c) shows the distributions for three incident directions $\omega = 45, 90, 135$. It can be confirmed that the red reflection, caused by the distribution out of specular reflection in the one-time-measuring method result, is the white noise, because such a red reflection is not seen in the 100-time-measuring method result.

Here, it is not natural that the noise appears only in the red color component. Mukaigawa et al. [22] have mentioned this kind of unnatural noise in a particular wavelength, caused by the wavelength dependence of the optical path in the measuring device. However, the problem on the device has not been solved in this research yet.

Next, I quantitatively evaluated the measured BRDFs of the simple method and multiplexing method. For this, I calculated their errors using the 100-times-measured BRDF as the ground truth. The PSNR (peek signal to noise ratio) results are shown in Fig. 5.1. In the Y components, there is little difference. However, in the Cb and Cr components, it can be seen
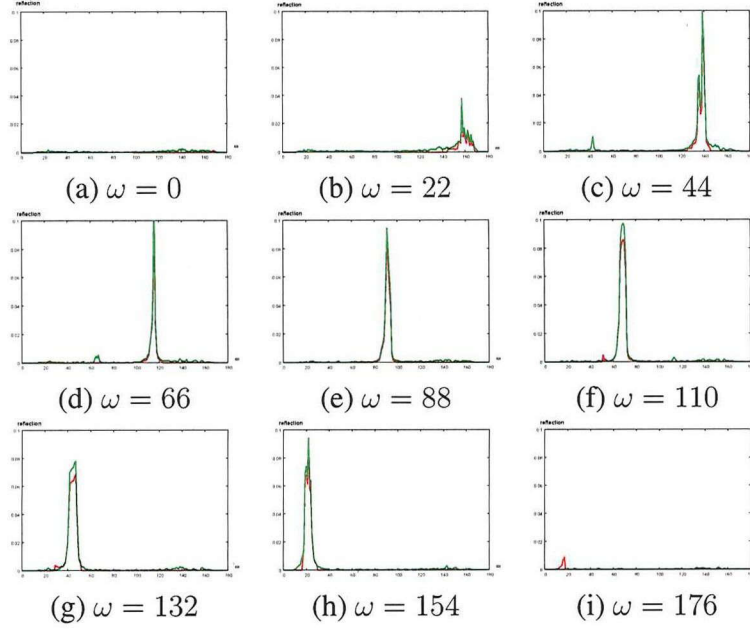
Figure 5.11: Comparison of restored reflections (red) with the ground truth (green).

that the measurement result in multiplexing method is improved. The improvement indicates reduction of red colored noise in the diffuse reflection distributions.

In the evaluations, I confirmed that the multiplexing method could not only reduce the measuring time but also improve the S/N ratio of the measured BRDF.

5.3.3 Measurement of Weak Specular Reflection

In the two previous experiments, it was confirmed that the multiplexing method is much useful to measure the reflectance property of strong specular objects like metal. Here, to evaluate the effectiveness for weak specular objects, the blue-colored paper was measured. When the object was illuminated in the direction $\omega = 120$, the reflected light was measured as shown in Fig. 5.3.2. In the distribution, the intensities in almost all of the direction have more than $1/10$ of the peak value. Hence, the illumination for the object cannot be multiplexed. In this result, I confirmed the limitation of the multiplexing method, explained in Sec.5.2.5.

5.3.4 Verification of Multiplexing Period

In this research, to estimate the range of specular distribution, I assumed that the specular reflection distribution is not spread to the range which is twice size of the range with intensties larger than $1/10$ of the peak value. However, the way to determine the range is empirically defined. So, I evaluated the validity by measurements for various materials. The sample materials

35
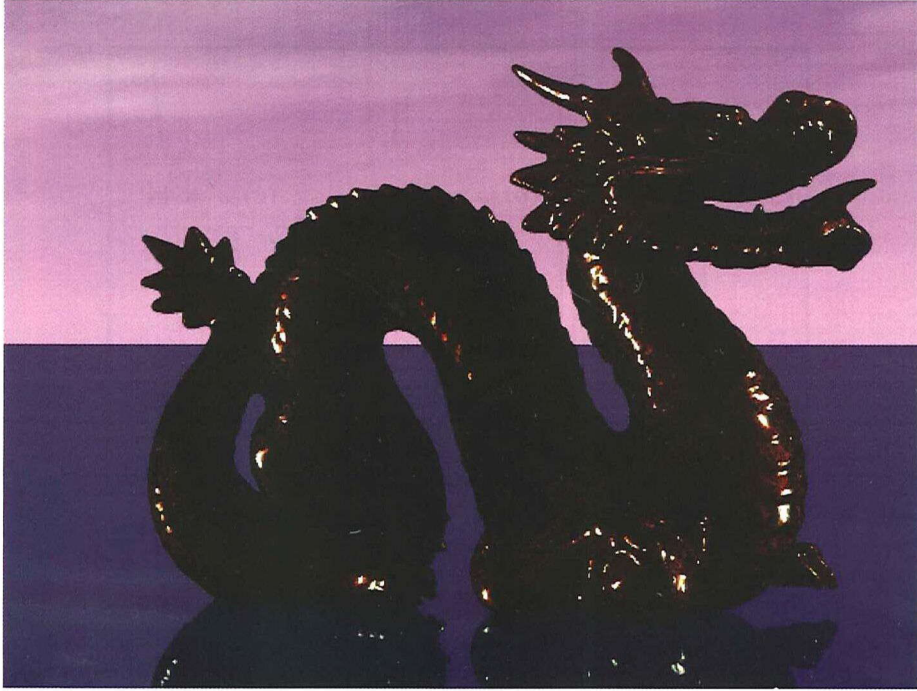
Figure 5.12: Single illumination.

are four types of plastic objects, eight types of metals, and five types of glossy papers, as shown in Fig. 5.3.4.

Figure 5.3.4 shows the ranges determined by a human observation and estimated by the proposed way. In the comparisons, the estimated range was tend to be larger than the human-observed range but the difference of the range size was not so large for most objects.

However, like a sample (a) in Fig. 5.3.4, if the estimated range is narrower than the actual range of specular reflection distribution, a BRDF might fail to measure. On the other hand, like a sample (b) in Fig. 5.3.4, if the estimated range is larger than the actual distribution range, the measuring time is not reduced so much though the measurement can work.

Here, to investigate in detail the reason why the estimation of distribution range failed, I checked the specular reflection distribution. As shown in Fig. 5.3.4 (a), the distribution for the underestimated range is asymmetry round the peak direction. On the right side of the peak direction, the intensities are rapidly decreasing. However, on the left side, the intensities keep low but non-zero values in wide range. On the other hand, As shown in Fig. 5.3.4 (b), the distribution for the overestimated range is very unstable because the intensities of the specular reflection is quite low and the noise in the diffuse reflection becomes relatively large. Hence, the range could not be successfully estimated in this case.

36
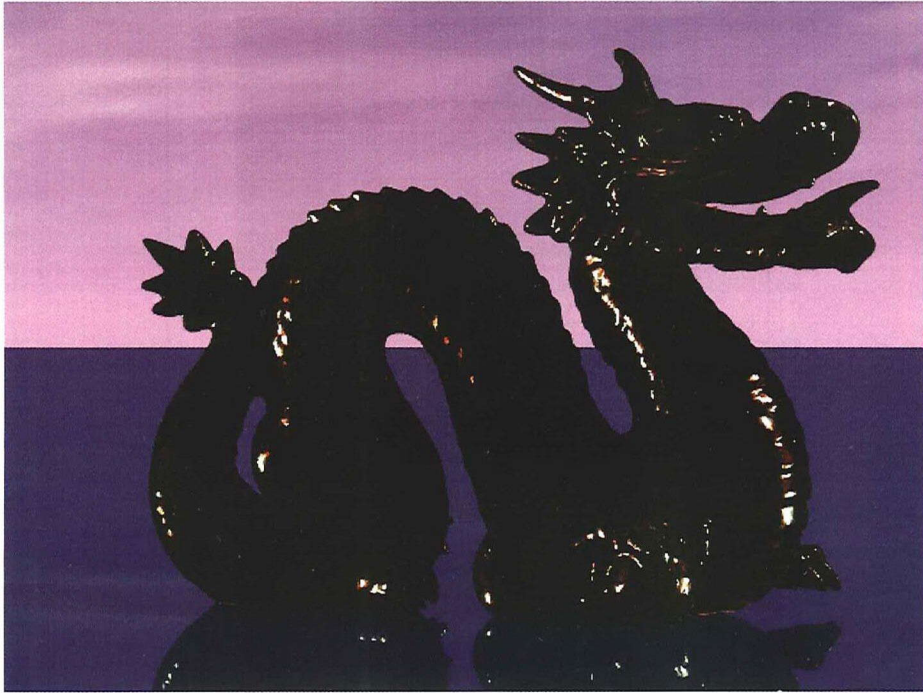
Figure 5.13: Composed multiple illumination.

From the above, it was confirmed that, for most objects, the proposed way to estimate the distribution range worked successfully, but it failed in the cases where the specular reflection distribution is asymmetry or the specular reflection is quite weak. In future works, the method to analyze the distribution in detail is needed in order to measure the objects with such hard properties.

reflection

(a) $\omega = 45$

reflection

(b) $\omega = 90$

reflection

(c) $\omega = 135$
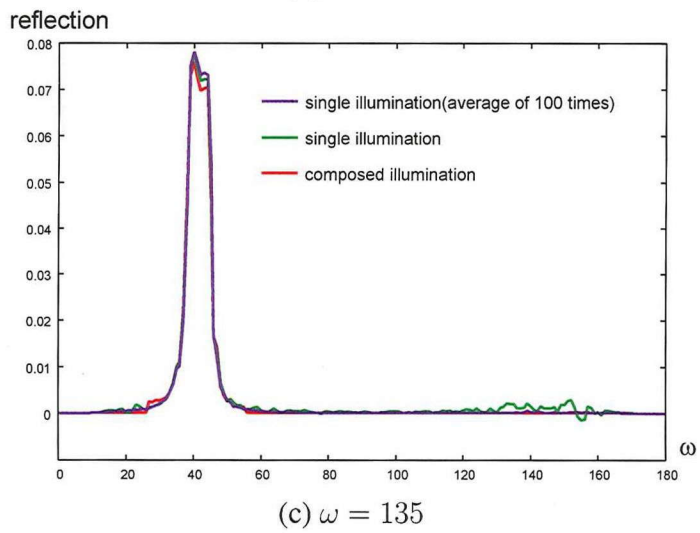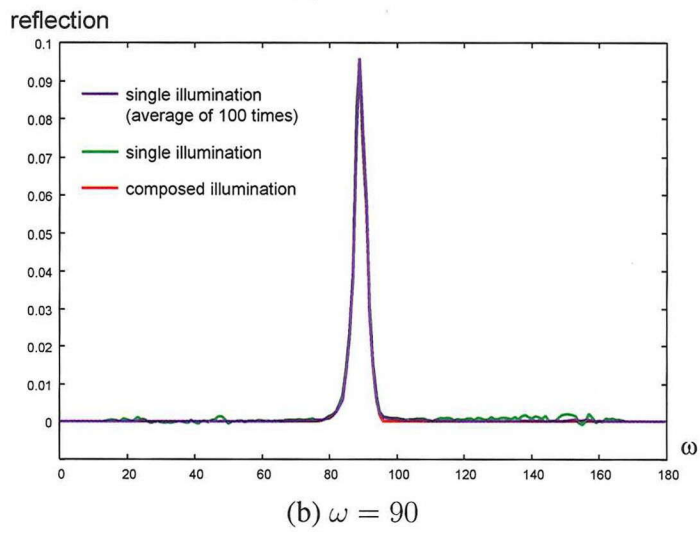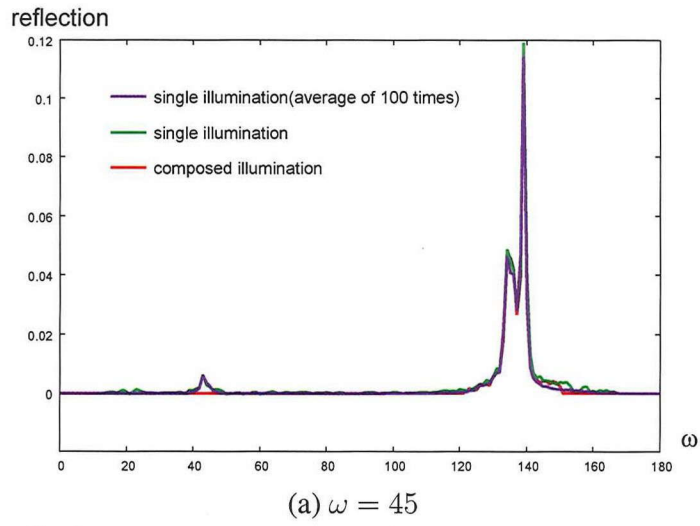
Figure 5.14: Effect of white noise reduction.
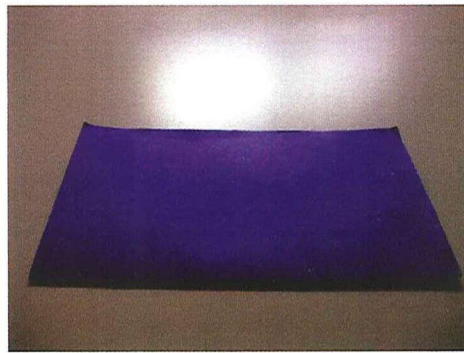
Figure 5.15: Blue paper.
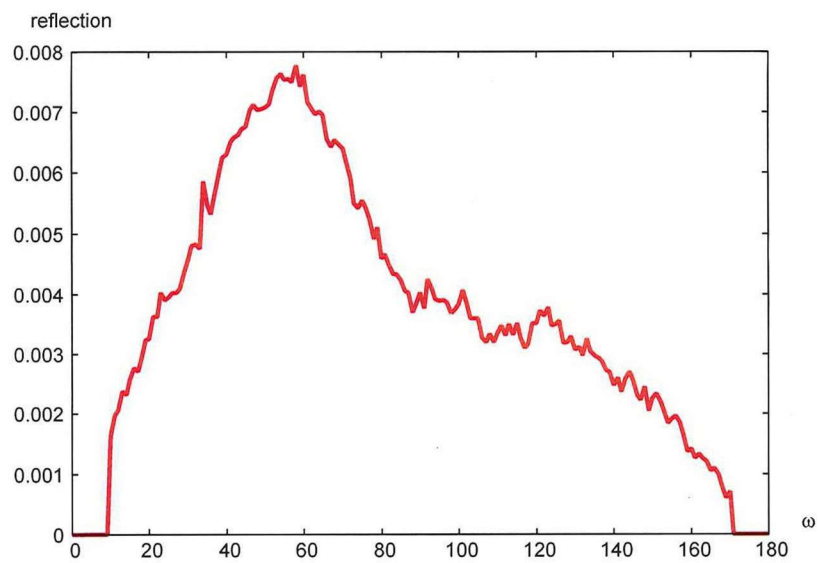
Figure 5.16: Distribution of reflection that illumination cannot be multiplexed.

Figure 5.17: Target samples for evaluating direction interval.
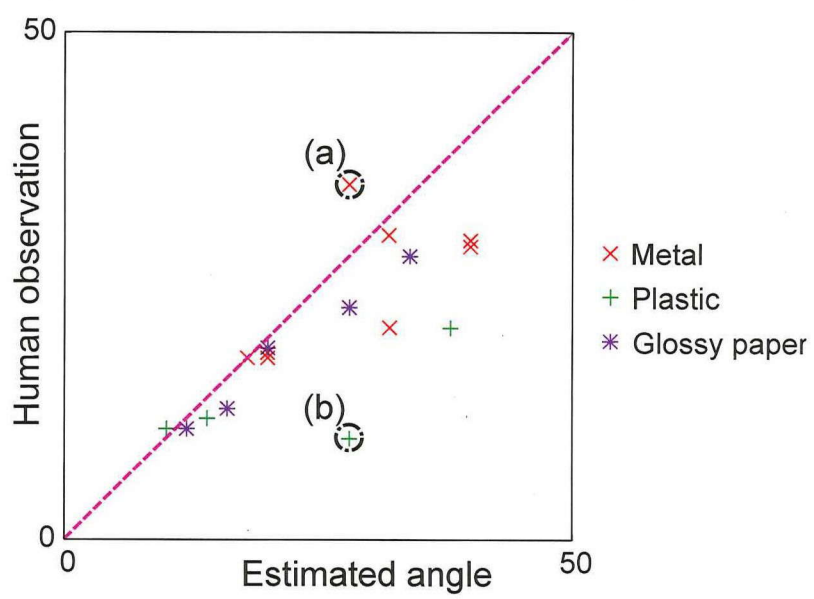
Figure 5.18: Relation between specular component spread angles of estimation and human observation.
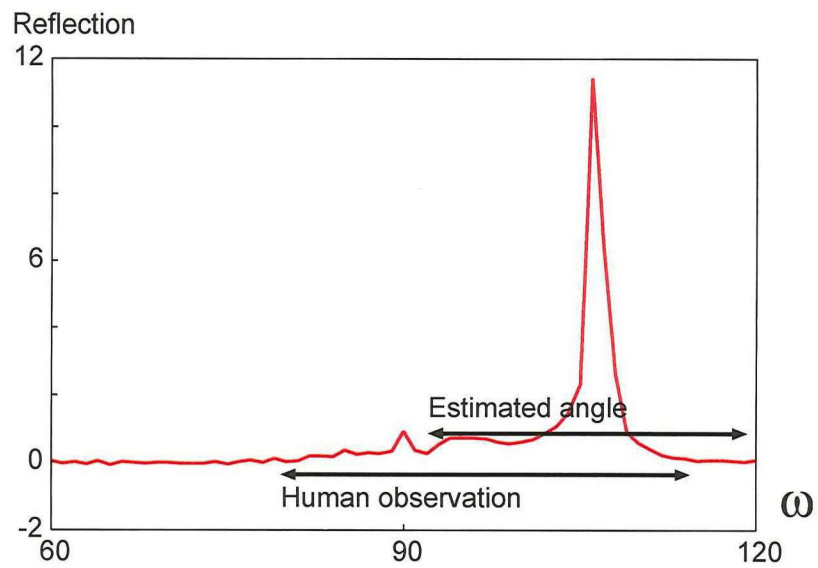
(a) Underestimate
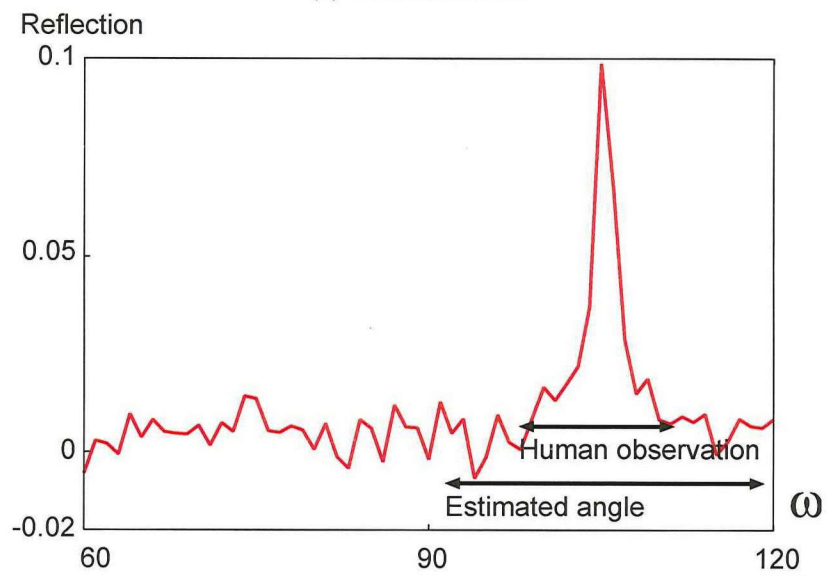
(b) Overestimate

Figure 5.19: Examples of incorrect estimation.

Chapter 6

Framework of 8-D Reflectance Field for Computational Photography

We often want to change the focusing or illumination conditions of photographs after they are captured, hence, some computational photography techniques have been proposed. For refocusing, the synthetic aperture [10] can tighten the depth-of-field or shift the focal plane. For relighting, the Light Stage[14] can generate images of the target object under arbitrary illumination conditions. Moreover, by controlling both focus and illumination, the confocal imaging[39] can clearly visualize a particular depth.

The formulation and the implementation of these computational photography techniques are optimized to a specific situation because they are specialized for different purposes in different research fields. Hence, the relationship between them has been unclear.

In this chapter, we introduce a unified framework to explain computational photography techniques based on an 8-D reflectance field (8DRF). The 8DRF represents the relationship between 4-D illumination and 4-D observation light fields. Since the 8DRF includes all information about illumination and reflection, the synthetic aperture, the image-based relighting, and the confocal imaging techniques can be explained as a computation of the 8DRF in the proposed framework. To confirm the validity of our framework, we have implemented these computational photography techniques on one system using the Turtleback Reflector [40], which is only one device for sampling an 8DRF over a hemisphere at uniform intervals.

6.1 Framework to Compute 8-D Reflectance Field

To formulate the computation of an 8DRF, I derive the framework to image the 8DRF. An image represents the appearance of the captured scene in two-dimensional data. So, the destination of the computation is to acquire a pixel value $I(D, C)$ for the given direction (D, C). In the

lens optics, the pixel intensity is given by integration of ray intensities passing through the lens. Thus, to acquire a pixel value, many rays in various directions are associated to the given direction (D, C) and the intensities are integrated. The integrated intensities are provided by a 4DLF of reflection from the scene. However, an 8DRF cannot directly represent a reflection light field because it gives us reflectance of the scene. So, at first, I compute the reflection light field by an 8DRF.

The reflection light field is the reflected light from the scene under an illumination condition. So, to compute the reflection 4DLF, an 8DRF $F(D_L, C_L, D_R, C_R)$ and an illumination light field $L(D_L, C_L)$ are needed. The reflection light field $R(D_R, C_R)$ can be derived as

$$R(D_R, C_R) \quad = \iint F(D_L, C_L, D_R, C_R) \cdot L(D_L, C_L) dD_L dC_L. \qquad (6.1)$$

As mentioned before, a lens focuses light rays from the scene at a point on an imaging plane. Here, the observed point also reflects many rays in the other directions as well as the captured rays. It is a selection of rays from the scene. So, I compute the selected rays $R'(D_R, C_R)$ to be integrated, as the masked reflection light field by a mask function $M(D_R, C_R$ as

$$R'(D_R, C_R) \quad = \quad R(D_R, C_R) \cdot M(D_R, C_R). \qquad (6.2)$$

Therefore, the target pixel intensity is computed as

$$I(D, C) \quad = \iint R'(D_R, C_R) dD_R dC_R. \qquad (6.3)$$

Totally, in the framework to compute an image from an 8DRF, I can get an image by a measured 8DRF of the scene $F(D_L, C_L, D_R, C_R)$, a given arbitaray illumination condition $L(D_L, C_L)$, and an optical ray selection $M(D_R, C_R)$ as

$$I(D, C) \quad = \iiiint F(D_L, C_L, D_R, C_R) \cdot L(D_L, C_L) \cdot M(D_R, C_R) dD_L dC_L dD_R dC_R. \qquad (6.4)$$

6.2 Implementations of Elemental Computational Photography

In this section, we formulate some computational photography techniques for the computation of an 8DRF in a unified framework. We unify the synthetic aperture, image-based relighting, and confocal imaging.

44

6.2.1 Synthetic Aperture Imaging

The synthetic aperture technique[10] realizes a virtual shallow depth-of-field (DoF). The imaging technique accumulates aligned multi-viewpoint images captured by a shifting camera or a camera array. Since the focal depth can be adaptively shifted by changing the aligned position, it is useful for refocusing.

The synthetic aperture can be formulated as a computation of an 8DRF. We synthesize an aperture A centered at D_R as shown in Fig.6.2. The focal plane is defined as a surface Π. The focused point S is derived by the intersection of the focal plane Π and a viewing ray passing through D_R along C_R. The mask function M, whether or not a ray passes through the point S and the aperture A:

$$M(D, C, S, A) = \begin{cases} 1 : \text{if the ray passes } S \text{ and } D \in A \\ 0 : \text{otherwise.} \end{cases} \tag{6.5}$$

The synthetic aperture imaging can be represented by integration of the eight dimensional reflectance field F with the mask function over the hemisphere. The following expression derives the intensity I of a pixel C_R on the image captured by a virtual camera with the aperture A and viewpoint D_R:

$$
\begin{aligned}
I(D_R, C_R, A, \Pi) = \iiiint & F(D_L, C_L, D'_R, C'_R) \cdot \\
& F_L(D_L, C_L) \cdot \\
& M(D'_R, C'_R, S, A) \cdot \\
& dD_L dC_L dD'_R dC'_R,
\end{aligned} \tag{6.6}
$$

where S is a function of D_R, C_R and Π. F_L is given as a constant 4DLF of illumination.

First, we evaluated the ability of the synthetic aperture using the prototype system. A textured paper was covered using an obstacle of yellow dense mesh, as shown in Figure 7.6(a). A white uniform pattern was projected onto the scene. Figure 7.6(b) shows the captured image from the real camera. This image includes 50 views corresponding to 50 virtual cameras. Because all the views are affected by the obstacle, it is difficult to see the texture of the paper. Figure 7.6(c) shows the change in appearance when the number of virtual cameras increases to synthesize a large aperture. Because our optical device can synthesize half the hemispherical aperture, the obstacle is completely blurred and the texture becomes clear with an increasing number of virtual cameras.

Figure 6.3 shows the result of the synthetic aperture on our framework using our 8DRF measuring device. This imaging technique synthesizes the shallow DoF images. The experimental scene consists of the textured film over the textured paper as shown in (a). Since the gap

(a) target scene   (b) captured image

1 view   2 views   3 views   4 views

20 views   30 views   40 views   50 views

(c) change of the aperture size
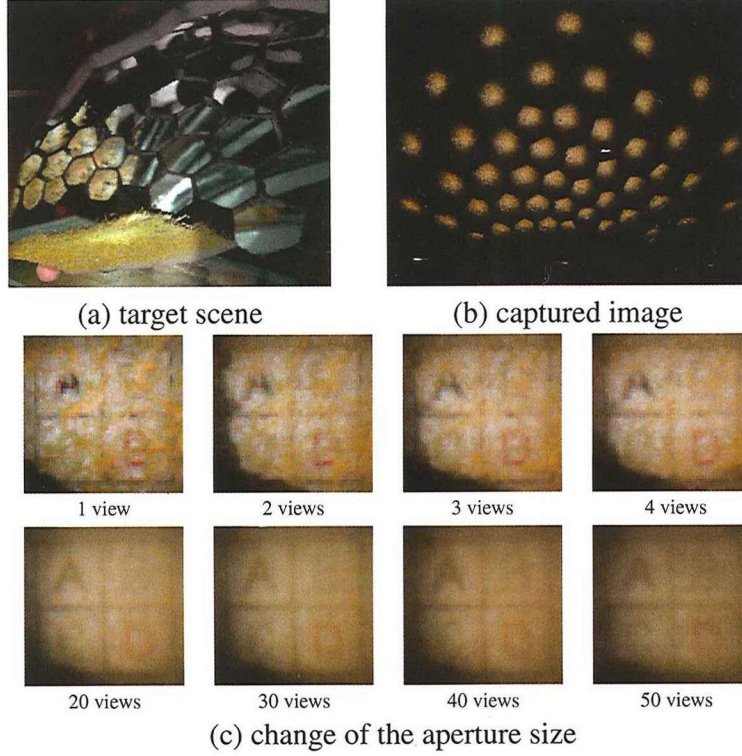
Figure 6.1: Results for synthetic aperture using our optical device.

between the two layers is only 1 mm, the two textures are mixed if a normal camera is used as shown in (b). The images (c) and (d) are the results of refocusing on the film and the paper. We can see that two layers are well separated. This confirms the synthetic aperture is successfully accomplished using the 8DRF measuring device.

6.2.2 Image-Based Relighting

The image-based relighting technique can generate a realistic image of a scene under arbitrary illumination[14]. The technique is achieved using a simple combination of the captured images under different illuminations.

This technique is also formulated on an 8DRF. Illumination of the scene is completely described by a four dimensional illumination light field F_L. For a camera fixed at D_R, as shown in Fig.6.4, the intensity I of the pixel C_R of the camera image can be expressed as:

$$I(D_R, C_R, F_L) = \iint F(D_L, C_L, D_R, C_R) \cdot F_L(D_L, C_L)dD_L dC_L. \tag{6.7}$$

The F_L can be given arbitrarily.

46
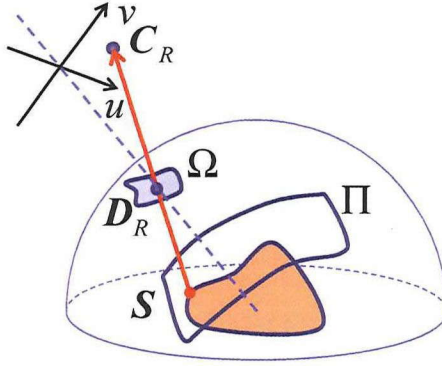
Figure 6.2: Synthetic aperture. This is achieved by an accumulation of intensities of rays passing through an aperture to make a target focal plane.

Figure 6.5 shows the results of the image-based relighting on our framework using the 8DRF measuring device. The target object is a metallic ring (a) which has complex reflectance properties. In general, it is difficult to synthesize a realistic view under arbitrary illumination by modeling the reflectance. The top row of (b) shows the illumination conditions[1]. Fifty pixel values were sampled for illumination because the used device has fifty light sources. The bottom row shows the synthesized images corresponding to the illumination conditions approximately generated by fifty point light sources.

6.2.3 Confocal Imaging

The confocal imaging technique is used in microscopy. It can clearly create an image at the depth of interest by simultaneously scanning the illumination and observation using a pinhole.

The confocal imaging can be formulated as a computation of an 8DRF because an 8DRF can synthesize a large aperture for both illumination and observation. Scanning a pinhole synthesizes a virtual aperture A at the center point D on a hemispherical surface. The target focal surface in the scene is given as Π.

The mask function M indicates whether the ray from a focused point S on the focal plane Π passes through the aperture A as shown in Fig.6.6.

$$M(\boldsymbol{D}, \boldsymbol{C}, \boldsymbol{S}, A) = \begin{cases} 1 : \text{if the ray passes } \boldsymbol{S} \text{ and } \boldsymbol{D} \in A \\ 0 : \text{otherwise} \end{cases} \tag{6.8}$$

The confocal imaging can be represented by integration of the 8DRF with the mask function. The following expression derives the intensity I of a pixel $\boldsymbol{C}_R$ on the image captured by a

---

[1]The images are Debevec's light probe images at `http://ict.debevec.org/~debevec/Probes/`

(a) scene setting

| (b) normal aperture | (c) $z = 0$ mm (synthetic) | (d) $z = 1$ mm (synthetic) |
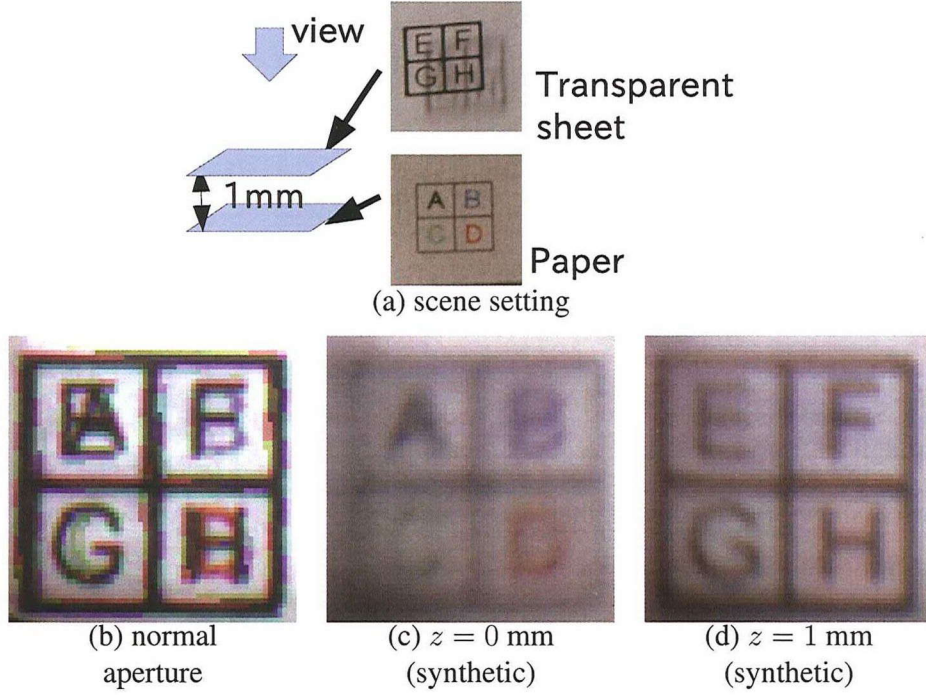
Figure 6.3: The results of the synthetic aperture. The scene consists of a textured film and textured paper 2 mm beneath it. In the normal aperture image, both the textures are mixed. In the synthetic images, the textures are separately focused and can be read.

virtual aperture A for both illumination and observation and the viewpoint $\boldsymbol{D}_R$:

$$
\begin{aligned}
I(\boldsymbol{D}_R, \boldsymbol{C}_R, A, \Pi) = \iiiint & F(\boldsymbol{D}_L, \boldsymbol{C}_L, \boldsymbol{D'}_R, \boldsymbol{C'}_R) \cdot \\
& M(\boldsymbol{D}_L, \boldsymbol{C}_L, S, A) \cdot \\
& M(\boldsymbol{D'}_R, \boldsymbol{C'}_R, S, A) \cdot \\
& d\boldsymbol{D}_L d\boldsymbol{C}_L . d\boldsymbol{D'}_R d\boldsymbol{C'}_R
\end{aligned}
\tag{6.9}
$$

Figure 6.7 shows the result of the confocal imaging on our framework using the 8DRF measuring device. The target scene consists of the target textured paper beneath an occluding orange mesh as shown in (a). In a view captured by a normal camera, the orange mesh occludes the texture as in (b). Although, as shown in (c), the synthetic aperture can blur the mesh, the texture is still unclear. The result of confocal imaging presents clear texture of the paper and less effect from the mesh as shown in (d).

48
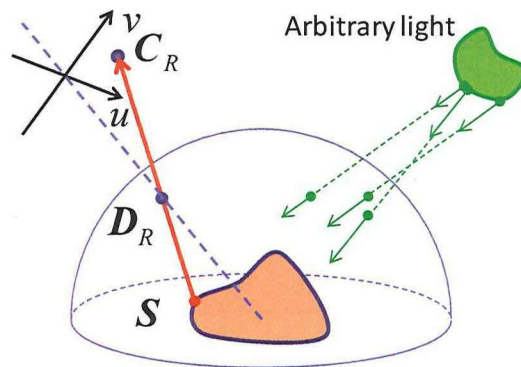
Figure 6.4: Image-based relighting. Given the illumination condition, the images can be synthesized from the corresponding observations in the 8DRF.

(a) object   (b) relighting results
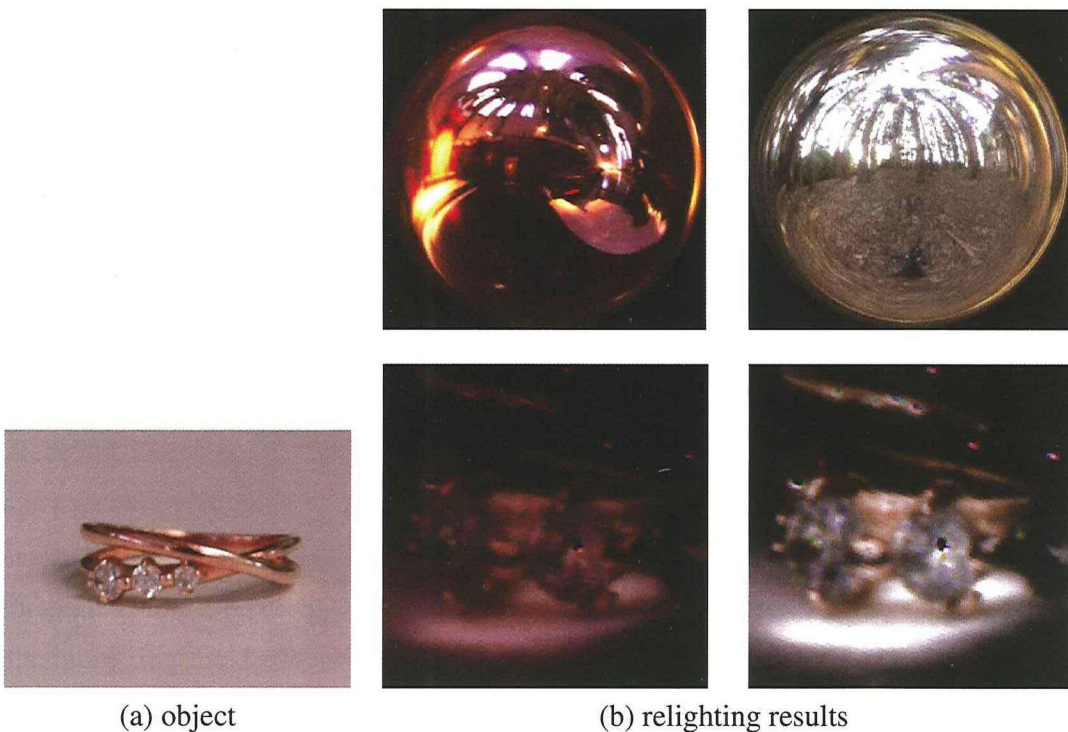
Figure 6.5: The results of the image-based relighting. For the given illuminations (top row), the corresponding appearances can be reproduced by simple computation of the 8DRF (bottom row).
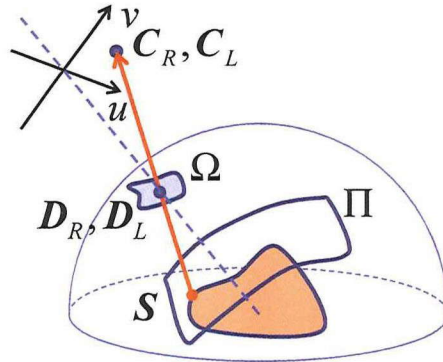
Figure 6.6: Confocal imaging. The observation and illumination have the same focal plane.

(a) scene

(b) normal view

(c) synthetic
aperture
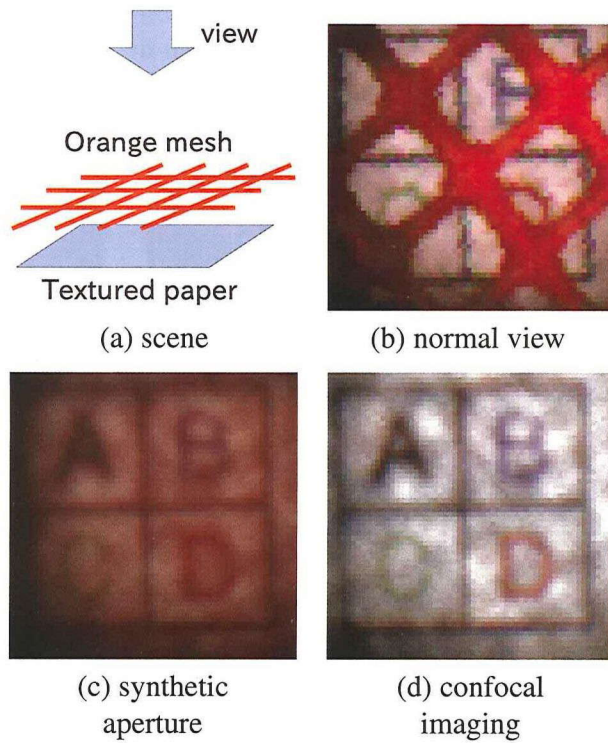
(d) confocal
imaging

Figure 6.7: The result of confocal imaging. The scene consists of the textured paper and overlapped orange mesh. In the normal view, the textured paper is partially occluded by the mesh. In the synthetic aperture image, the texture is recognizable because the mesh is significantly blurred, while the orange color remains. In the confocal image, the texture becomes clear because the mesh is significantly blurred and less illuminated.

Chapter 7

Hemispherical Confocal Imaging

7.1 Introduction

Significant effort has been made to obtain cross-sectional views of 3-D scenes. Real scenes often include obstacles such as scattering materials or opaque occluders. To visualize the cross-sectional views clearly as if the scene is sliced by a plane, only a particular depth must be illuminated, and haze due to scattering and attenuation should be removed.

The simplest way to observe a particular depth is to use a large aperture lens. The large aperture makes the depth of field (DOF) shallow, and the region outside the DOF is blurred. The synthetic aperture method [10] mimics a large virtual aperture by combining many small apertures. However, the obstacles are still bright and visible, even though they are blurred. The confocal imaging method [39] simultaneously scans two confocal pinholes over a particular depth. Because both the illumination and the observation are focused, clear cross-sectional views are obtained. While still visible, the obstacles are darkened and blurred, and the scanning requires long measuring times.

Recently, Levoy et al. [20] proposed a new imaging technique that combines the synthetic aperture method with the confocal imaging method. Since this technique is based on light field analysis, only a particular depth can be illuminated without scanning. However, the synthesized aperture size is relatively small because the rectangular mirrors are aligned as a 2D array. Furthermore, unwanted effects such as scattering and attenuation remain.

In this research, we propose a novel imaging method called *hemispherical confocal imaging*. To improve the imaging performance of synthetic aperture confocal imaging [20], we designed a *turtleback reflector* which is a polyhedral mirror used to approximate a hemispherical aperture with a 180° FOV (field of view). We introduce *focused high frequency illumination* using the turtleback reflector with a projector. This method can eliminate scattering at the fo-
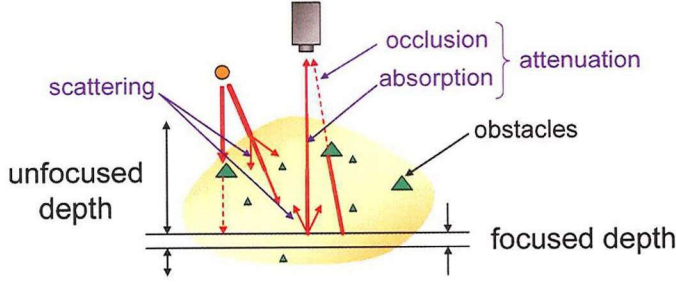
Figure 7.1: Illumination and reflection in a 3-D scene. It is difficult to observe a particular depth due to scattering and attenuation.

Table 7.1: Comparison of several imaging methods.

	unfocused depth	scanning	scattering
Synthetic aperture	bright	unnecessary	remaining
Confocal imaging	darken	necessary	remaining
Synthetic aperture confocal imaging[20]	unilluminated	unnecessary	remaining
Confocal imaging with descattering [37]	darken	necessary	reduced
Our hemispherical confocal imaging	unilluminated	unnecessary	reduced

cused depth, and makes the unfocused depth almost invisible. We also introduce *factorization* of the observed views to eliminate attenuation.

Contribution

- By using the new optical device, the unfocused depth becomes almost invisible, the scattering is eliminated and the measurement is very fast, because no scanning is required.

- We have designed the *turtleback reflector*, which is a polyhedral mirror circumscribed in an ellipsoid. The combination of the turtleback reflector, a projector, and a camera can synthesize a hemispherical wide aperture. The optical device can also be used for measuring the complete 8-D reflectance field on the hemisphere.

- A new analysis of the 8-D reflectance field is introduced to obtain clear views. This analysis removes the unnecessary effects of scattering and attenuation in captured images.

7.2 Hemispherical confocal imaging

Let us assume that a 3-D scene is illuminated by a light source and observed by a camera as shown in Figure 7.1. Even if the camera is focused on a particular depth in the scene, the
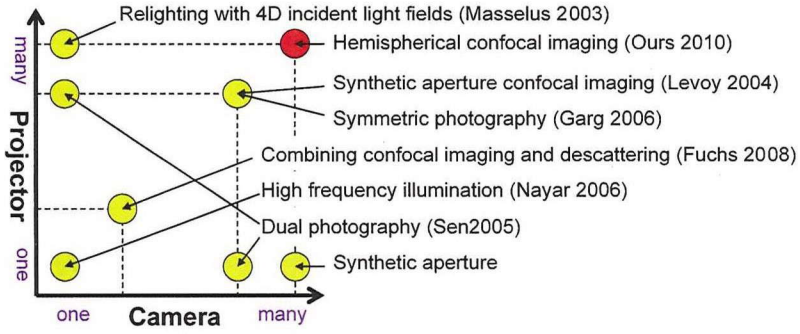
Figure 7.2: The numbers of projectors and cameras of several imaging methods which use projector(s) and camera(s) for reflection analysis or reflectance field measurement.

captured image includes reflections from the entire scene. To observe the particular depth, only that depth should be illuminated. This means that both the illumination and the observation should have a shallow DOF.

Even if we succeed in illuminating only the particular depth, clear views cannot be observed. The major reasons for this are *scattering* and *attenuation*. The scattering is caused by multi-bounce reflections in the translucent media, which cause the views to become blurred. The attenuation is caused by *occlusion* due to obstacles or *absorption* due to low transparency media. Under this attenuation, the illumination becomes nonuniform and the reflections are partially darkened. The following four functions are required to obtain clear views of a particular depth in a 3-D scene.

(a) The DOF should be as shallow as possible.

(b) Only the particular depth of interest should be illuminated.

(c) Scattering should be eliminated.

(d) Attenuation should be eliminated.

To satisfy these requirements, we propose *hemispherical confocal imaging* consisting of (1) a specially designed *turtleback reflector*, (2) *focused high frequency illumination*, and (3) *factorization* of observed views.

The turtleback reflector with coaxial camera and projector synthesizes a hemispherical aperture for both illumination and observation to satisfy (a). The focused high frequency illumination eliminates reflections from the unfocused depth and global reflection to solve (b) and (c). We then factorized the observed views into masking, attenuation, reflected light, illuminance, and texture terms to solve for (d). The advantages and disadvantages and the numbers of projectors and cameras for several imaging methods are summarized in Table 7.1 and Figure 7.2.

53

Although we explained that unfocused depths are 'unilluminated' by the synthetic aperture confocal imaging and our hemispherical confocal imaging, the depths are actually illuminated, but these illuminations are eliminated by subtractive calculation. Hence, image noise may increase.

7.3 Focused high frequency illumination

7.3.1 Illumination and reflection in a 3-D scene

To analyze the reflectance field in a 3-D scene, we need to know how light illuminates points in a scene, and how the reflections are observed. We divide the 3-D scene into a set of small voxels. Let L be an illumination on the scene, and $R_k(L)$ be an image component that consists of a set of reflected and scattered lights from the k-th voxel under the illumination L as shown in Figure 7.3 (a). Because the observed image of the entire scene by a camera is expressed as a sum of the reflected and scattered lights from all voxels, the image is represented by $\sum_i R_i(L)$.

Illuminations and reflections can be regarded as the sum of the direct and global components[38]. As shown in Figure 7.3 (b), the illumination can be decomposed into direct L^D and global illuminations L^G as

$$L = L^D + L^G. \tag{7.1}$$

Similarly, the reflection can also be decomposed into the direct $R_k^D(L)$ and global reflections $R_k^G(L)$. The R_k^D is recorded as the pixel intensity at the intersection of the image plane and the line between the k-th voxel and the camera, while the R_k^G is recorded as the part of the intensity of other pixels as shown in Figure 7.3 (a).

The image component $R_k(L)$ can be decomposed into the direct and global components as

$$R_k(L) = R_k^D(L) + R_k^G(L). \tag{7.2}$$

It is easy to assume that the R_k is a linear function by disabling the gamma correction of the camera. Hence, the observed image can be modeled as the sum of four components by

$$\sum_i R_i(L) = \sum_i R_i^D(L^D) + \sum_i R_i^D(L^G) + \sum_i R_i^G(L^D) + \sum_i R_i^G(L^G). \tag{7.3}$$

54

(a) rays on image plane

(b) four types of ray

(c) focused illumination

(d) classification of voxels
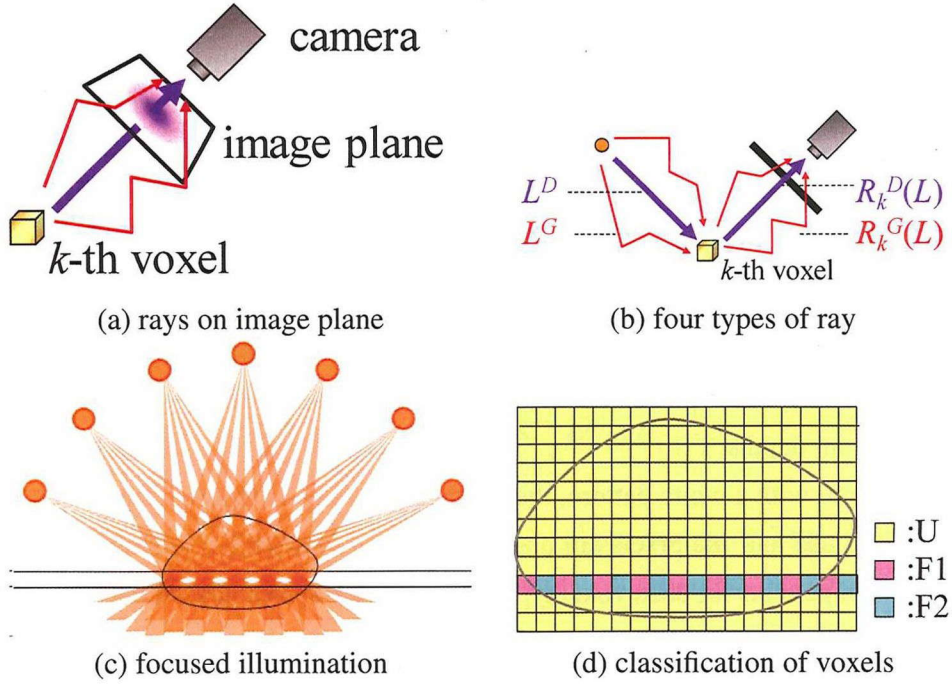
Figure 7.3: Focused high frequency illumination. The high frequency patterns are focused only on the particular depth. The projection is blurred out of the DOF.

7.3.2 Focused illumination by multiple projectors

To obtain clear views of a particular depth in a 3-D scene, only that depth should be illuminated. Any global illuminations and global reflections should be eliminated to reduce scattering in the media. That is, direct reflections by direct illuminations, $R_k^D(L^D)$, from the particular depth should be measured separately.

Fuchs et al.[37] proposed the descattered confocal imaging technique to capture a clear view of a particular depth in scattering media. They combined the focused illumination technique proposed by Levoy et al.[20] and the high frequency illumination technique proposed by Nayar et al.[38]. They captured clear descattered images by line scanning confocal imaging. However, this technique could not deal with reflections from opaque objects in the unfocused depth. The reflections were introduced as the floodlit contribution by Levoy et al.[20]. They removed them using many observations under a lot of random pattern illuminations.

Here, we propose a new imaging method, called *focused high frequency illumination* (**FHFI**), based on descattered confocal imaging [37]. Our technique can remove the floodlit contribution and requires only constant measurement time. The FHFI uses a lot of projectors placed over a wide range on a hemisphere.

For the FHFI, high frequency checkerboard patterns are projected from each projector. The positions of the white and black pixels are aligned at the depth as shown in Figure 7.3 (c). This means that the high frequency illumination is focused only at a particular depth. The voxels in the scene are classified into unfocused voxels U, focused and illuminated voxels $F1$, and focused but unilluminated voxels $F2$ as shown in Figure 7.3 (d).

It is noted that synthetic aperture illumination with regular patterns like checkerboards often cause artifacts of periodic patterns at depths other than the focal plane [41]. This artifact occurs when the projected patterns are accidentally aligned at different depths. This problem can be reduced by the hemispherical placement of the virtual projectors because projected patterns do not align at different depths.

When compared with a white pattern, the average intensity of the high frequency illumination is darker because half the pixels are black. Table 7.2 shows the relative intensities of the four reflection components for each voxel type. The global illumination to each voxel decreases by half. The direct illumination to U voxels also decreases by half because the projected patterns are blurred. Therefore, the floodlit contribution decreases by half under the FHFI using the turtleback reflector. The $F1$ voxels receive full direct illumination, while the $F2$ voxels receive no direct illumination. By combining these differences, $\sum_{i \in F1 \cup F2} R_i^D(L^D)$ which enables only direct components from voxels at the focused depth to be separated.

Let I_P be a captured image when voxels of $F1$ are illuminated but voxels of $F2$ are not illuminated. Let I_N be a captured image when the inverse pattern is projected. Then, these images can expressed as

$$I_P = \sum_{i \in F1} R_i \left(L^D + \frac{L^G}{2} \right) + \sum_{i \in F2} R_i \left(\frac{L^G}{2} \right) + \sum_{i \in U} R_i \left(\frac{L^D + L^G}{2} \right), \quad (7.4)$$

$$I_N = \sum_{i \in F1} R_i \left(\frac{L^G}{2} \right) + \sum_{i \in F2} R_i \left(L^D + \frac{L^G}{2} \right) + \sum_{i \in U} R_i \left(\frac{L^D + L^G}{2} \right). \quad (7.5)$$

The absolute difference of two intensities in I_P and I_N is then calculated for each pixel. Since this is a pixel-wise process, the pixel intensities at coordinates (x, y) in I_P, I_N, and $R(L)$ are expressed as $I_P(x, y)$, $I_N(x, y)$, and $R(L, x, y)$. The absolute difference I_D is calculated by

$$
\begin{aligned}
I_D(x, y) &= \left| I_P(x, y) - I_N(x, y) \right| \\
&= \left| \sum_{i \in F1} R_i(L^D, x, y) - \sum_{i \in F2} R_i(L^D, x, y) \right| \\
&= \left| \sum_{i \in F1} R_i^D(L^D, x, y) + \sum_{i \in F1} R_i^G(L^D, x, y) \right. \\
&\qquad \left. - \sum_{i \in F2} R_i^D(L^D, x, y) - \sum_{i \in F2} R_i^G(L^D, x, y) \right|.
\end{aligned}
\quad (7.6)
$$

Table 7.2: Relative intensities of four reflection components for each voxel type.

	$R_k^D(L^D)$	$R_k^D(L^G)$	$R_k^G(L^D)$	$R_k^G(L^G)$
U (unfocused)	1/2	1/2	1/2	1/2
F1 (focused and illuminated)	1	1/2	1	1/2
F2 (focused and unilluminated)	0	1/2	0	1/2

If we can assume a locally homogeneous surface, the global component does not change even if the phase of the high frequency pattern shifts [37][38]. Therefore,

$$\sum_{i \in F1} R_i^G(L^D, x, y) \simeq \sum_{i \in F2} R_i^G(L^D, x, y). \tag{7.7}$$

Moreover, $\sum_{i \in F1} R_i(L^D, x, y)$ and $\sum_{i \in F2} R_i(L^D, x, y)$ are exclusive. That is, when the voxels of $F1$ are illuminated, the former becomes large while the latter becomes zero and vice versa. Hence,

$$\begin{aligned} I_D(x, y) &= \left| \sum_{i \in F1} R_i^D(L^D, x, y) - \sum_{i \in F2} R_i^D(L^D, x, y) \right| \\ &= \sum_{i \in F1} R_i^D(L^D, x, y) + \sum_{i \in F2} R_i^D(L^D, x, y) \\ &= \sum_{i \in F1 \cup F2} R_i^D(L^D, x, y). \end{aligned} \tag{7.8}$$

This means that only the particular depth ($F1 \cup F2$) can be directly illuminated without global illuminations, and only the direct reflections can be measured without global reflections. As shown in Table 7.1, our method does not illuminate the unfocused depth. Because no scanning is necessary, the measurement is fast. Furthermore, scattering, which is a major global component in translucent media, is eliminated.

7.4   Factorization of the observed views

7.4.1   Attenuation of incident and reflected light

By the FHFI introduced in the previous section, only the focused depth is illuminated and global components such as scattering are eliminated. However, the obtained view may still be unclear because illumination and reflected light attenuate. The reason for the attenuation is the *occlusion* and *absorption* as shown in Figure 7.1.

These are similar but different optical phenomena. Occlusion directly interrupts reflected light by opaque obstacles. Hence, it causes very dark regions with sharp edges in the observed

(a) Observations (b) Illuminations
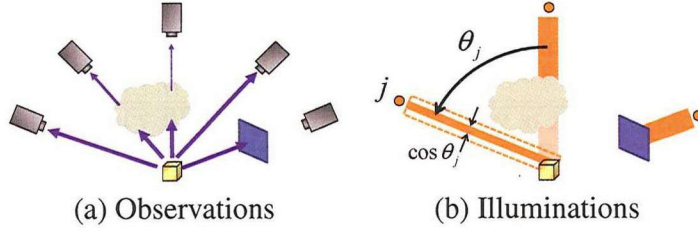
Figure 7.4: Attenuation effects.

image. On the other hand, absorption decreases lighting powers by low transparency media. It causes smooth unevenness in the observed image. To obtain a clear view at a particular depth of the scene, the optical effects of occlusion and absorption should be eliminated.

7.4.2 Factorization using multiple images

The attenuation occurs in both observation and illumination. However, if the observation and illumination are coaxial, the attenuation effects are the same. Hence, we can estimate the attenuation of the observation.

When a region in a captured image is dark, we cannot directly know why the reflectance is low or the illumination is weak. It is difficult to eliminate attenuation effects using only a single image. Fortunately, the scene is observed from many virtual cameras. Even if some lights are not observed from a camera, other cameras may observe the scene without attenuation as shown in Figure 7.4(a). Hence, we try to estimate texture that is not affected by attenuation based on observation from multiple cameras.

To factorize the observed intensities into reflected light and the attenuation, we assume that surface reflections can be expressed by the Lambert model. That is, the observed brightness is independent of the viewing angle. We assume that there are K virtual cameras and each camera has N pixels. Let O_{ij} be the intensity of the i-th pixel in the j-th camera. In our model, the observed intensities are factorized as

$$O_{ij} = M_{ij} A_{ij} R_i. \tag{7.9}$$

Here, M_{ij} is the *masking term* which has a value of 0 or 1. If the light is occluded by obstacles, the value becomes 0 otherwise it becomes 1. A_{ij} is the *attenuation term*, which expresses light attenuation due to absorption. R_i is the *reflected light term* which expresses reflected light of the particular depth under attenuated illumination. It is noted that only the reflected light term is independent of the viewing direction, assuming Lambertian reflection. Figure 7.5 illustrates this relationship.

58
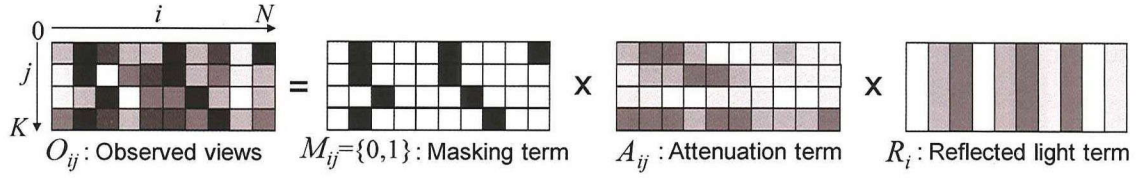
Figure 7.5: Concept of factorization. The observed intensities are factorized into masking, attenuation, and reflected light terms to reduce attenuation.

The flow of the factorization process is as follows

STEP-1: First, the masking term is decided. Since unfocused depths are not illuminated by the FHFI, obstacles can easily be distinguished using a simple threshold. After making the decision on the masking term, the following processes are conducted for pixels satisfying $M_{ij} = 1$.

STEP-2: The initial attenuation term is decided as $A_{ij} = 1$.

STEP-3: The reflected light term is calculated. Ideally, a unique reflected light should be estimated despite the different camera j, but the observed intensities vary. This kind of problem is often seen in stereoscopy[42], so we used a median filter in a similar fashion by $R_i = \text{Median}(O_{ij}/A_{ij})$.

STEP-4: The attenuation term is updated by $A_{ij} = O_{ij}/R_i$ to satisfy Eq.(7.9).

STEP-5: The attenuation term is smoothed using a Gaussian function, because the attenuation varies smoothly over the 3-D scene. After this, return to **STEP-3** and repeat until the texture term does not change.

Using this factorization process, the observed views are decomposed to three terms and we can obtain the reflected light of the particular depth without attenuation of the observation.

Although the reflected light term R_i is estimated, it includes the attenuation effects of the illumination. Hence, we estimate the texture term T_i, which is independent of the illumination, by eliminating attenuation effects in the reflected light term. First, a maximum illuminance on the surface is estimated. The maximum illuminance is the illuminance when there are no obstacles. The illuminance from the j-th virtual projector weakens in proportion to $\cos\theta_j$, where θ_j is the zenith angle as shown in Fig.10(b). Here, we can assume that the illuminance is uniform over the surface by assuming that the observation area is small. Hence, the maximum

illuminance L_i^m for i-th pixel can be expressed by the sum of illuminance from all virtual projectors as follows,

$$L_i^m = \sum_j \cos \theta_j. \tag{7.10}$$

Since the j-th virtual projector and the j-th virtual camera are placed at the same position, we can regard the attenuation term A_{ij} as the attenuations of the illumination from the j-th virtual projector on the i-th pixel. Hence, the sum of the attenuated illuminance L_i^a is expressed as

$$L_i^a = \sum_j M_{ij} A_{ij} \cos \theta_j. \tag{7.11}$$

Therefore, the texture term T_i is restored by

$$T_i = R_i L_i^m / L_i^a. \tag{7.12}$$

Through these processes, the observed views are decomposed into a masking term, attenuation term, illuminance, and texture term. In this texture term, both the attenuation effects of the observation and the illumination are eliminated.

7.4.3 Stability of the masking term

Pixel-wise masking is often used for merging multiple images. Wilburn et al.[41] used a mask to reconstruct an alias-free synthetic aperture image. They decided on a mask based on the variance of corresponding pixels.

On the other hand, we used a simple threshold. In general, shadow regions are not perfectly black because of global illumination. However, our FHFI can effectively eliminate the global components in advance. Hence, pixel intensities in shadow regions become close to zero, and the regions can be segmented stably.

Our factorization process strongly depends on the Lambert model. We assume that intensities observed by multiple cameras become constant if there is no attenuation. Hence, if the diffuse assumption is violated and strong specular reflections are observed, the factorization does not work well.

7.5 Experiments

7.5.1 Synthetic aperture using virtual cameras

First, we evaluated the ability of the synthetic aperture using the prototype system. A textured paper was covered using an obstacle of yellow dense mesh, as shown in Figure 7.6(a). A white

(a) target scene   (b) captured image

1 view   2 views   3 views   4 views

20 views   30 views   40 views   50 views

(c) change of the aperture size
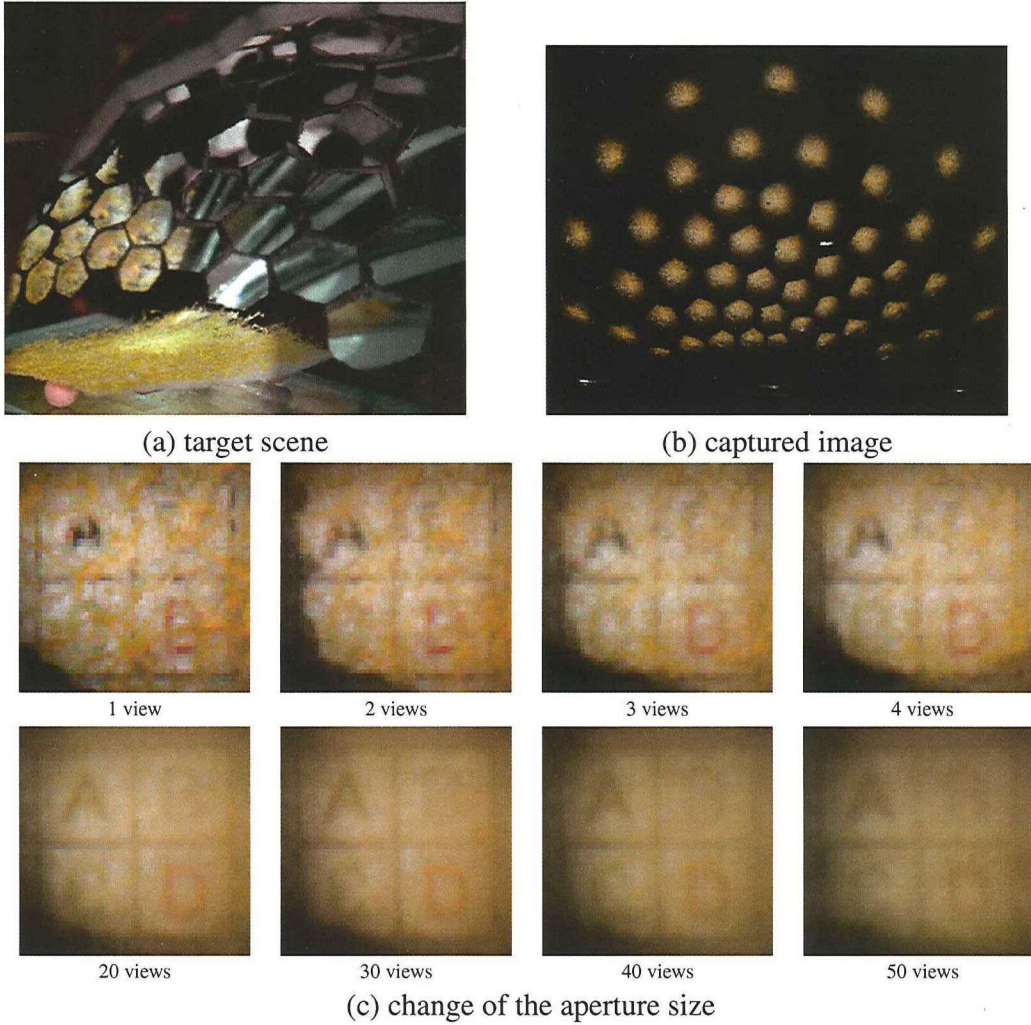
Figure 7.6: Results for synthetic aperture using our optical device.

uniform pattern was projected onto the scene. Figure 7.6(b) shows the captured image from the real camera. This image includes 50 views corresponding to 50 virtual cameras. Because all the views are affected by the obstacle, it is difficult to see the texture of the paper. Figure 7.6(c) shows the change in appearance when the number of virtual cameras increases to synthesize a large aperture. Because our optical device can synthesize half the hemispherical aperture, the obstacle is completely blurred and the texture becomes clear with an increasing number of virtual cameras.

7.5.2 Shallow DOF

The turtleback reflector can produce an extremely large aperture using the synthetic aperture technique. To evaluate the DOF, a textured paper is captured using a hemispherical synthetic

| z=0.5mm | z=0.4mm | z=0.3mm | z=0.2mm | z=0.1mm | z=0.0mm |
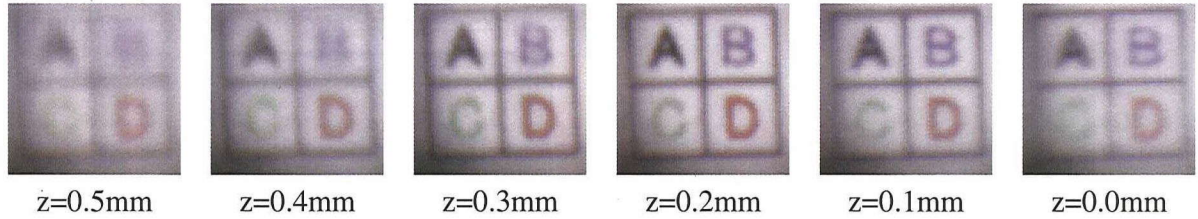
Figure 7.7: Sweeping focal plane.

aperture. We synthesize an aperture focused on a plane with 0.1mm increments between $z = 0.0$mm and $z = 0.5$mm. As shown in Figure 7.7, the image at $z = 0.2$mm is the most focused and the images at $z = 0.0$mm and $z = 0.4$mm are blurred explicitly. Therefore, the DOF provided by the turtleback reflector is about 0.4mm. This DOF is not very shallow because we implemented only half of the turtleback reflector. However, we confirmed the ability to make a shallow DOF.

7.5.3 Descattering by focused high frequency illumination

Next, we confirmed that the FHFI is effective for descattering in a 3-D volume. The textured paper in Figure 7.8(a) is covered by a sponge as in (b). Since the sponge scatters lights strongly, edges are blurred.

In theory, only two illumination patterns are needed for the FHFI. However, the illuminated pattern becomes blurred at the edges. Hence, we used checkered patterns, in which white and black are replaced every three pixels and shifted the pattern by one pixel. In total, 18 illumination patterns are projected from the virtual projectors so that these patterns are aligned on the paper. As Nayar et al.[38] did, we took maximum and minimum intensities for each pixel position in the 18 images. Then, the difference image can be obtained.

Figure 7.8 (c) shows the direct component obtained by the FHFI. We can see that scattering in the 3-D scene is reduced and the contrast is improved. To show how much the contrast was improved, we analyzed the intensity profiles of the images as shown in Figure 7.8 (d). This graph shows intensity profiles along a horizontal line at the mid height of the images. The central region from 20 to 40 corresponds to the black part of the spade figure. We can see that the contrast was improved by descattering. The descattering effect is not perfect, which is attributed to the low resolution of the virtual projectors in the current prototype system.

(a)

(b)

(c)

(d) Intensity profiles
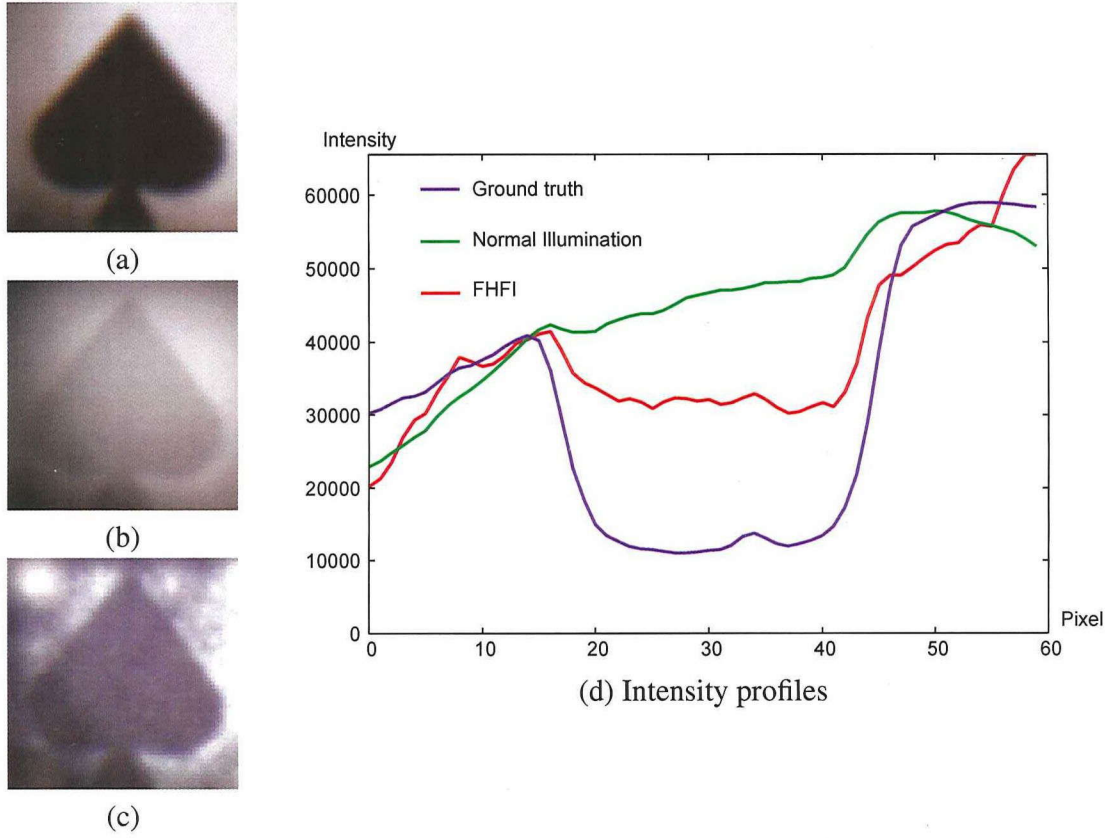
Figure 7.8: Descattering by focused high frequency illumination.

7.5.4 Factorization of the observed views

We confirmed the ability to visualize a particular depth in a 3-D scene by combining the FHFI and the factorization. The factorization reduces attenuation effects of occlusion and absorption. Hence, we evaluated them separately.

In the first experiment, we used a scene with occluders. Figure 7.9(a) shows the scene where an orange mesh covers a textured paper, and (b) shows all views from the virtual cameras under normal illumination[1]. By simply averaging these views, a synthetic aperture image can be generated, as shown in (c). Although the obstacle is blurred, the orange color of the mesh affects the paper. Confocal imaging [39] can generate a better image as shown in (e) because the orange mesh is less illuminated.

The mesh becomes dark under the FHFI because it is not illuminated, while the paper is bright, as shown in (h). By averaging these views, the dark mesh is blurred and the orange color correctly disappears, as shown in (d). However, there are uneven dark regions due to

---

[1]Although there are 50 mirror patches, only 48 patches were used because two patches were misaligned.

(a) scene   (b) views under normal illumination   (g) groundtruth

(c) synthetic aperture   (d) FHFI w/o factorization   (e) confocal imaging   (f) reflected light term

(h) direct reflection   (i) masking term

(j) attenuation term   (k) illuminance   (l) texture term
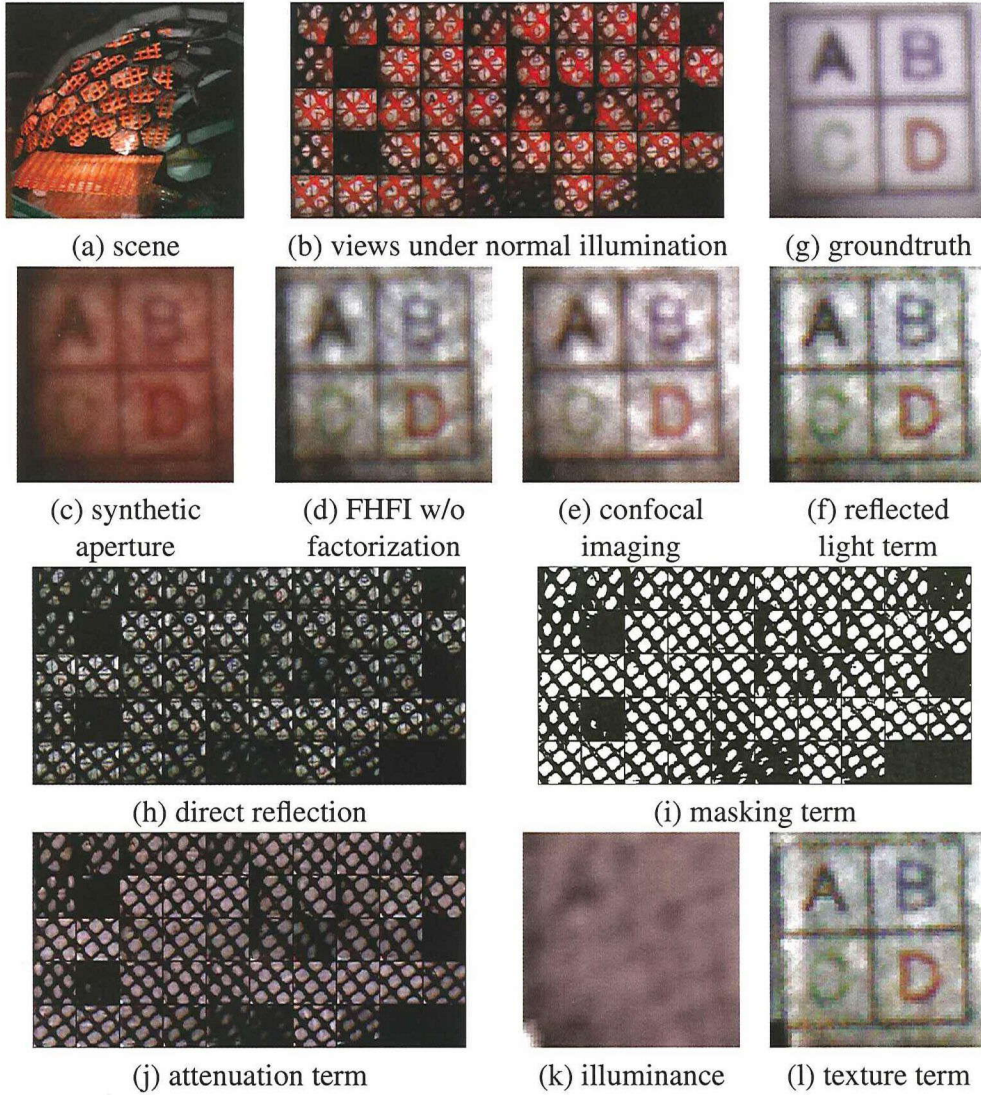
Figure 7.9: Result of the combination of the FHFI and the factorization with an occluded scene.

attenuation. The factorization decomposes the observed views (h) into the masking term (i), the attenuation term (j), and the reflected light term (f). We then estimate the illuminance (k) and the texture term (l) using these decomposed terms. We see that the attenuation is reduced, especially around the letters of the black 'A' and the red 'D', since the occlusion due to the mesh is regarded as masking. On the other hand, comparing (l) with (f), the attenuation is too reduced under the letter 'B' because of the inaccurate masking term. Around the edges of obstacles, the masking term cannot be accurately estimated due to the low resolution of the virtual cameras.

While the difference compared with the ground truth image (g) that was captured without the orange mesh is not small, we confirmed that the image without the DOF can be made to

<div style="text-align:center">

(a) ground truth   (b) direct reflection   (c) w/o factorization

(d) normal view   (e) attenuation term   (f) texture term

</div>
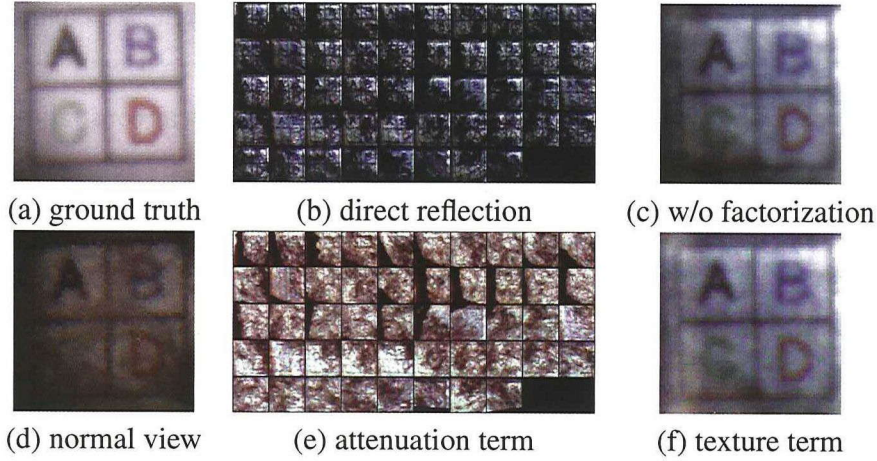
Figure 7.10: Result of the combination of the FHFI and the factorization with an absorbed scene.

almost disappear by hemispherical confocal imaging.

In the second experiment, we used a scene with an inhomogeneous translucent absorber. A target scene consists of a textured paper of Figure 7.10 (a) with cotton waste on the paper. A normal view (d) is unevenly attenuated. In the direct components obtained by the FHFI, attenuation still remains as in (b). Figure 7.10 (e) shows the attenuation term, and expresses smooth change of absorption and (f) shows the texture term.

While the attenuation and texture terms were factorized, the effectiveness was weak. Figure 7.10 (c) shows a simple average of (d). The difference between (c) and (f) is small. One of the possible reasons is calibration errors. In fact, the hemispherical synthetic aperture and the FHFI effectively improved the appearance. However, accurate geometric calibration of virtual cameras is required for the factorization. Another reason is that the FHFI did not completely remove scatterings due to the low resolution, while the factorization assumes that images have no scattering.

7.6 Limitations

- The resolution of the virtual projectors and cameras is low, because the imaging areas of the real projectors and cameras are divided into the virtual areas.

- The observable area is narrow because all of the projectors must illuminate and all of the cameras must observe a common area. To enlarge the area, a large turtleback reflector is necessary, and it may be difficult to construct.

- The factorization is basically an ill-posed problem. For example, we cannot distinguish between two different scenes in which a red texture is covered with a colorless film and a white texture is covered with a red film. Some empirical constraints such as the smoothness of attenuation are necessary.

7.7 Summary

We propose a new method of hemispherical confocal imaging. This new imaging technique enables us to observe clear views of a particular depth in a 3-D scene. The turtleback reflector designed here can divide the imaging areas so that a projector and a camera mimic a number of virtual projectors and cameras surrounding the scene. The combination of the focused high frequency illumination and the factorization can illuminate only the particular depth of interest, and eliminate scattering and attenuation. We have constructed a prototype system and confirmed the principles of the hemispherical aperture, descattering, and factorization.

Chapter 8

Conclusion

In this dissertation, I addressed the difficulty in using 8-D reflectance fields as imaging components because of the high dimensionality. So far, 8-D reflectance fields are well known as carrying useful information that can represent appearances of a target scene under varying illumination. Ideally, with 8-D reflectance fields we can create an image of a scene under arbitrary illumination in an arbitrary focus and viewpoint.

Here, I proposed fundamental techniques for imaging using 8-D reflectance fields. The fundamental techniques are how to measure, how to compute, and how to image. For how to measure, I designed the turtleback reflector and developed multiplexed illumination for rapid measurements. For how to compute, I established a unified framework for computing 8-D reflectance fields.

Although 8-D reflectance fields are very beneficial, there are no practical measuring devices. To measure 8-D reflectance fields, the measuring directions should cover a whole hemisphere with a target scene at the center. If the purpose is not to measure 8-D reflectance fields but analyze the scene properties, Levoy et al. [20] have already developed a device that uses synthetic aperture confocal imaging. However, this device cannot measure 8-D reflectance fields on a hemisphere. This is why I have developed the turtleback reflector, which is the optics to measure 8-D reflectance fields. The turtleback reflector is used with a projector and camera, and consists of fifty mirrors designed to uniformly locate fifty virtual projectors and cameras on a hemisphere. In the system, 8-D reflectance fields can be uniformly measured, although the resolutions are lower than for a simple device in which a projector and camera are rotated around a scene, taking a long time. Thus, the turtleback reflector I propose is the first device for measuring 8-D reflectance fields.

To understand 8-D reflectance fields, I first considered what they can represent on the slices and on the whole. Although reflectance fields can represent appearances of a 3-D scene, properties that represent how materials reflect incident light can be described as the lower-dimensional

slices of 8-D reflectance fields. The reflectance property of materials has been used to make realistic computer graphics, where even lower-dimensional reflectance properties are very useful. Moreover, the reflectance is used to verify the painted or finished surface of industrial products because it shows the change in detail for different illumination directions, so the reflectance gives micro-scale surface information. It is through measuring 8-D reflectance fields that we obtain these useful properties. That is why I have pursued practical use of 8-D reflectance fields.

One of the problems with measuring 8-D reflectance fields is the device design. This problem is solved as mentioned above. Another of the problems is the measuring method. The measurement takes a very long time because of the amount of variation in illumination. The large variation depends on the complexity of the surface reflectance of objects in the target scene. So, first of all, I described a rapid measuring method for isotropic BRDFs. Light reflected from a material surface is distributed in various directions even for an incident light ray. Thus, the reflection distributions for some incident light rays overlap in most directions and cannot be easily separated. So, I separately analyzed the diffuse and specular reflection distributions. The diffuse reflection distributions can overlap as far as the incident directions are known because the distribution can be assumed to be uniform in every direction. On the other hand, the specular reflection distributions do not overlap but tend to be in a narrow angular range. Therefore, illumination directions can be multiplexed as far as the specular reflection distributions do not overlap. Here, I showed that the reflectance fields could be measured by multiplexed illumination.

Even if the reflectance fields can be measured, we cannot directly make an image from the data without computations. So, a number of imaging techniques have been developed that use light fields or reflectance fields. For example, a 4-D light field can be used to create a re-focused image where the focused depth can be changed after capturing the scene, using the synthetic aperture imaging technique. Using a reflectance field with more than four dimensions, one can synthesize the varying appearances of the scene under various illumination conditions. However, the techniques are not uniformly described because they are individually proposed for different devices. Because of this, we have not had guidelines on which dimensions are important for specific applications. So, I unified some computational photography techniques that generate a scene appearance, as a computation of 8-D reflectance fields. To do this, I presented an imaging method to compute an image from a combination of an 8-D reflectance field, given illumination light fields, and mask function that achieves the optics used in the system for each target technique. I also confirmed, with the results from using the turtleback

reflector system, that the framework well duplicates the synthetic aperture imaging technique, image-based relighting technique, and confocal imaging technique. Ultimately, I proposed the first imaging framework for computing 8-D reflectance fields.

For many imaging techniques, an entire 8-D reflectance field is not needed. However, using an entire 8-D reflectance field is beneficial to analytical imaging techniques. To show the benefit, I have developed hemispherical confocal imaging that makes a clear image of a particular depth in a scene with a hemispherical aperture, focused high frequency illumination, and factorization of the multi-view image. To make a shallow depth of field, a hemispherical aperture is synthesized with the turtleback reflector. The focused high-frequency illumination can theoretically remove the reflection and scattering light in and out of the target depth of field by focusing high-frequency patterns from virtual projectors on the depth and significantly blurring them elsewhere. Thus, when the pattern is shifted, the reflection from the target depth is changed, while that from the non-target depths is not changed. So, the target reflection can be acquired as a difference between the reflections. The illumination assumes that the patterns are significantly blurred out of the depth of field. The hemispherical aperture realizes this. The differential reflection has the specific characteristic that only a part of the scene in the depth of field, is illuminated. Because the appearances of obstacles are dark, the occluded region in the multi-view image can be easily segmented. Thus, the appearances of the target depth can be analyzed to correct the illuminance of the depth, exploiting the co-axial installations of a virtual projector and camera; when the observation from the virtual camera is occluded in a region, the illumination from the virtual projector is similarly occluded. This way, the 8-D reflectance field can be used in imaging techniques by making the observation easier to analyze using arbitrary illumination conditions.

So far, the techniques for 8-D reflectance fields have not been addressed. However, with these techniques, using 8-D reflectance fields has become feasible and practical for various applications. I have made guidelines about how to use 8-D reflectance fields for imaging.

8.1   Discussion

How far can the unified framework compute?

In my framework, I addressed the computation of an 8-D reflectance field for imaging an appearance of a scene with arbitrary viewpoint and focusing under arbitrary illumination. Here, the 8-D reflectance field includes every optical effect such as interreflections between objects in the scene that are, in computer graphics, hard to compute because of the geometric and

photometric information needed. However, the optical effects are not separately stored in the reflectance fields. Therefore, although the effects can be reproduced in the computed images, all the effects are composed and cannot be simply separated. For example, if we want just interreflections, we have to analyze the interreflected scene and cannot use the framework for this purpose. Ultimately, we can use the framework only for creation of appearances of a target scene.

Is the turtleback reflector the best device for measuring 8-D reflectance fields?

The turtleback reflector can make many virtual projectors and cameras on a hemisphere. It is relatively easy to install many projectors and cameras on a hemisphere. Actually, the virtual projectors and cameras are on a hemisphere, but the arrangement density and resolution are not very high. If a scene is large, the turtleback reflector becomes larger. In this case, actually installing projectors and cameras can be easier than implementing the turtleback reflector. The turtleback reflector is appropriate for relatively small measuring systems in which the target objects are smaller than a projector, because the minimum mirror in my reflector is almost the same size as the target scene. If the mirror is larger than a projector, installing the mirror becomes more difficult than installing the projector. Eventually, the size of the target scene decides whether the turtleback reflector is the best device for measuring 8-D reflectance fields.

The turtleback reflector, however, helps to reduce the computational cost. If many projectors and cameras are actually arranged, they should be controlled by many computers. Here, because virtual projectors and cameras can be controlled by one computer through a projector and camera, fewer computers are needed. Moreover, the virtual arrangement helps synchronization. All the virtual projectors are perfectly synchronized because they consist of parts of a projection pattern by a real projector. The virtual cameras are synchronized for the same reason. Therefore, with the turtleback reflector, only a real projector and camera needed to be synchronized. This is much less difficult than synchronizing many computers, projectors, and cameras.

However, the turtleback reflector system is inferior to the actually installed system with respect to the resolution of acquired 8DRFs. So, the reflector might not be suitable for high-resolution measurements in which a high-resolution projector and camera cannot provide virtual projectors or cameras with sufficient resolutions.

The turtleback reflector is easier to use with a measuring system. One reason is that it can be more easily implemented if a target scene is relatively small. Another reason is that it can

be more easily controlled because there are fewer synchronized instruments. Therefore, the turtleback reflector is not always the best device but is useful for measuring 8DRFs.

Is the 8-D reflectance field really useful?

For the same amount of information, the 8-D reflectance field has less resolution than reflectance fields with fewer dimensions. It is a trade-off between dimensionality and resolution of reflectance fields. Moreover, the turtleback reflector unfortunately discards much of the resolution of the combined real projector and camera. So, it might seem wasteful.

Actually, in this dissertation, the 8-D reflectance fields have not been measured in the best way, where the resolutions of a real projector and camera are fully leveraged. However, the 8DRF has a powerful ability to analyze scene appearances even if the resolutions are low. The hemispherical confocal imaging, proposed in Chapter 7, is the evidence. The imaging technique needs an 8DRF or a device that can measure 8DRFs. It is based on four-dimensional illumination and analysis of four-dimensional observation under focused high frequency illumination. Hence, it will not work with reflectance fields of fewer than eight dimensions.

To summarize, although the 8DRF might seem wasteful because the resolution decreases in exchange for the high dimensionality, it is very useful even if the resolution is low.

8.2 Future Work

Clarifying the relationships among proposed techniques

Although I proposed a unified framework to compute 8-D reflectance fields, the relationships among computational photography techniques have not been completely clarified. If they are clarified, then it may be possible to clarify remaining fields for which combinations of dimensions for illumination and observation have not been implemented.

I suggested hemispherical confocal imaging was one of the remaining fields. The addressed field is clear because not all eight dimensions have been analyzed. There are many techniques that analyze multi-view images, while there are fewer techniques that analyze high-dimensional illuminations. So, there are probably still some remaining fields of reflectance fields with less than eight dimensions.

Making an entire device precisely

The implemented turtleback reflector is a prototype that implements only a half of my design. So, the reflector arranges virtual projectors and cameras on half a hemisphere. For an entire system that has not been implemented, as shown in Figure 3.4, two turtleback reflectors

should be implemented and combined with two pairs of a real projector and camera for virtual arrangements all over a hemisphere.

The alignment and calibration of the prototype system are briefly done. Although the system has worked well nevertheless, that is probably because the system measures low-resolution data, and the misalignment and rough calibration have less influence on the resulting image. Thus, if high-resolution projectors and cameras are used in the entire system, the precision of the alignment and calibration should be high.

Rapid measurement of 8-D reflectance fields

Finally, I mention the rapid measurement of 8-D reflectance fields because it is difficult to measure them with simple methods because of the high dimensionality. Thus, rapid measurement is a future work. The difficulty of measuring reflectance fields is that the illumination cannot be easily multiplexed. Multiplexed reflection can be restored for each illumination only when the reflection distributions for each illumination do not overlap. Such multiplexed illumination has been proposed for isotropic BRDFs in Chapter 5. In the multiplexing technique, I exploited dichromatic reflection to avoid overlapping reflection by separately considering the reflection as diffuse and specular reflections. The isotropic BRDF is a three-dimensional reflectance field, so it is a simple case in which the illuminated and observed scenes are the same point.

However, the 8-D reflectance field expresses the appearances of more complicated 3-D scenes. The multiplexing technique cannot be simply applied to measurements of 8-D reflectance fields. Symmetric photography has been proposed [19] to reduce the measuring time. However, the device used cannot have the projectors and cameras covering either a whole hemisphere or a large area of a hemisphere. Moreover, the technique assumes the target objects to be approximately planar for estimating reflection distributions for each illumination. Both our and their multiplexed techniques assume a tendency for reflection distributions.

Recently, compressive sensing has been used to acquire a reflectance field. This technique does not assume the target reflectance fields to have any measurementtendencies despite using multiplexed illumination. The tendencies are considered in the restoration process. Therefore, the 8-D reflectance field will probably be measured rapidly with compressive sensing.

Reference

[1] A. Levin, R. Fergus, F. Durand, and W. T. Freeman, "Image and Depth from a Conventional Camera with a Coded Aperutre," in *Proc. SIGGRAPH2007*, 2007.

[2] R. Raskar, A. Agrawal, and J. Tumblin, "Coded Exposure Photography: Motion Deblurring using Fluttered Shutter," in *ACM SIGGRAPH 2006*, 2006.

[3] J. Kim, R. Horstmeyer, I.-J. Kim, and R. Raskar, "Highlighted Depth-of-Field Photography: Shining Light on Focus," *ACM Transactions on Graphics*, vol. 30, no. 3, 2011.

[4] H. Li, S.-C. Foo, K. E. Torrance, and S. H. Westin, "Automated three-axis gonioreflectometer for computer graphics applications," *Optical Engineering*, vol. 45(4), May 2006.

[5] G. J. Ward, "Measuring and Modeling Anisotropic Reflection," in *Proc. SIGGRAPH'92*, pp. 255–272, 1992.

[6] K. J. Dana and J. Wang, "Device for convenient measurement of spatially varying bidirectional reflectance," *J. Opt. Soc. Am. A, Vol.21, Issue 1*, pp. 1–12, 2004.

[7] Y. Mukaigawa, K. Sumino, and Y. Yagi, "High-speed measurement of brdf using an ellipsoidal mirror and a projector," in *Proc. IEEE International Workshop on Projector-Camera Systems (PROCAMS2007)*, 2007.

[8] A. Ghosh, S. Achutha, W. Heidrich, and M. O'Toole, "BRDF Acquisition with Basis Illumination," in *Proc. ICCV2007*, 2007.

[9] M. Levoy and P. Hanrahan, "Light Field Rendering," in *Proc. SIGGRAPH'96*, pp. 31–42, 1996.

[10] V. Vaish, B. Wilburn, N. Joshi, and M. Levoy, "Using Plane + Parallax for Calibrate Dense Camera Arrays," in *Proc. CVPR 2004*, 2004.

[11] E. H. Adelson and J. Y. Wang, "Single Lens Stereo with a Plenoptic Camera," *IEEE Tran. on PAMI*, pp. 99–106, 1992.

[12] J. Unger, A. Wenger, T. C. Hawkins, A. Gardner, and P. Debevec, "Capturing and Rendering With Incident Light Fields,"

[13] A. Veeraraghavan, R. Raskar, A. Agrawal, A. Mohan, and J. Tumblin, "Dappled Photography: Mask Enhanced Cameras for Heterodyned Light Fields and Coded Aperture Refocusing," in *Proc. SIGGRAPH2007*, 2007.

[14] P. Debevec, T. Hawkins, C. Tchou, H.-P. Duiker, W. Sarokin, and M. Sagar, "Acquiring the Reflectance Field of a Human Face," in *Proc. SIGGRAPH2000*, pp. 145–156, 2000.

[15] P. Sen, B. Chen, G. Garg, and S. R. Marschner, "Dual Photography," in *Proc. SIGGRAPH2005*, pp. 745–755, 2005.

[16] V. Masselus, P. Peers, and P. Dutré, "Relighting with 4D Incident Light Fields," in *Proc. SIGGRAPH2003*, pp. 613–620, 2003.

[17] W. Matusik, H. Pfister, A. Ngan, P. Beardsley, R. Ziegler, and L. McMillan, "Image-Based 3D Photography using Opacity Hulls," in *Proc. SIGGRAPH2002*, pp. 427–437, 2002.

[18] G. Müller, G. H. Bendels, and R. Klein, "Rapid Synchronous Acquisition of Geometry and Appearance of Cultural Heritage Artefacts," in *The 6th International Symposium on Virtual Reality, Archaeology and Cultural Heritage (VAST)*, pp. 13–20, 2005.

[19] G. Garg, E.-V. Talvala., M. Levoy, and H. P. A. Lensch, "Symmetric Photography : Exploiting Data-sparseness in Reflectance Fields," in *Proc. EGSR2006*, pp. 251–262, 2006.

[20] M. Levoy, B. Chen, V. Vaish, M. Horowitz, I. McDowall, and M. Bolas, "Synthetic Aperture Confocal Imaging," in *Proc. SIGGRAPH2004*, pp. 825–834, 2004.

[21] O. Cossairt, S. K. Nayar, and R. Ramamoorthi, "Light Field Transfer: Global Illumination Between Real and Synthetic Objects," Aug 2008.

[22] Y. Mukaigawa, K. Sumino, and Y. Yagi, "Multiplexed Illumination for Measuring BRDF using an Ellipsoidal Mirror and a Projector," in *Proc. of Asian Conference on Computer Vision (ACCV2007)*, pp. 246–257, 2007.

[23] I. Sato, T. Okabe, Y. Sato, and K. Ikeuchi, "Appearance Sampling for Obtaining a Set of Basis Images for Variable Illumination," in *Proc. ICCV2003*, pp. 800–807, 2003.

[24] P. Peers and P. Dutré, "Inferring Reflectance Functions from Wavelet Noise," in *Proc. the 16th Eurographics Symposium on Rendering*, pp. 173–182, 2005.

[25] D. Donoho, "Compressed sensing," *IEEE Transactions on Information Theory*, vol. 52(4), pp. 1289–1306, April 2006.

[26] E. Candès, J. Romberg, and T. Tao, "Robust uncertainty principles: Exact signal reconstruction from highly incomplete frequency information," vol. 52(2), pp. 489–509, February 2006.

[27] E. Candès and J. Romberg, "Quantitative robust uncertainty principles and optimally sparse decompositions," vol. 6(2), pp. 227–254, April 2006.

[28] P. Peers, D. Mahajan, B. Lamond, A. Ghosh, W. Matusik, R. Ramamoorthi, and P. Debevec, "Compressive Light Transport Sensing," *ACM Transactions on Graphics*, January 2009.

[29] R. Ng, M. Levoy, M. Brédif, G. Duval, M. Horowitz, and P. Hanrahan, "Light Field Photography with a Hand-held Plenoptic Camera," in *Stanford Tech Report CTSR 2005-02*, 2005.

[30] A. Levin, S. W. Hasinoff, P. Green, F. Durand, and W. T. Freeman, "4D Frequency Analysis of Computational Cameras for Depth of Field Extension," in *Proc. SIGGRAPH2009*, 2009.

[31] D. Lanman, R. Raskar, and G. Taubin, "Modeling and Synthesis of Aperture Effects in Cameras,"

[32] N. Kusumoto, S. Hiura, and K. Sato, "Uncalibrated Synthetic Aperture for Defocus Control," in *Proc. CVPR2009*, 2009.

[33] T. Treibitz and Y. Y. Schechner, "Active Polarization Descattering," pp. 385–399, 2009.

[34] J. Kim, D. Lanman, Y. Mukaigawa, and R. Raskar, "Descattering Transmission via Angular Filtering," in *Proc. ECCV2010*, pp. 86–99, 2010.

75

[35] S. G. Narasimhan, S. K. Nayar, B. Sun, and S. J. Koppal, "Structured Light in Scattering Media," in *Proc. ICCV2005, Vol 1*, pp. 420–427, 2005.

[36] J. Gu, S. K. Nayar, E. Grinspun, P. Belhumeur, and R. Ramamoorthi, "Compressive Structured Light for Recovering Inhomogeneous Participating Media," in *Proc. ECCV2008*, pp. 845–858, 2008.

[37] C. Fuchs, M. Heinz, M. Levoy, H.-P. Seidel, and H. P. A. Lensch, "Combining Confocal Imaging and Descattering," *Computer Graphics Forum, Special Issue for the Eurographics Symposium on Rendering 2008*, vol. 27, pp. 1245–1253, June 2008.

[38] S. K. Nayar, G. Krishnan, M. D. Grossberg, and R. Raskar, "Fast Separation of Direct and Global Components of a Scene using High Frequency Illumination," in *Proc. SIGGRAPH2006*, pp. 935–944, 2006.

[39] M. Minsky, "Microscopy Apparatus." US Patent 3013467, 1961.

[40] Y. Mukaigawa, S. Tagawa, J. Kim, R. Raskar, Y. Matsushita, and Y. Yagi, "Hemispherical Confocal Imaging using Turtleback Reflector," in *Proc. ACCV2010*, pp. 331–344, 2010.

[41] B. Wilburn, N. Joshi, V. Vaish, E.-V. Talvala, E. Antunez, A. Barth, A. Adams, M. Horowitz, and M. Levoy, "High Performance Imaging Using Large Camera Arrays," in *Proc. SIGGRAPH2005*, pp. 765–776, 2005.

[42] V. Vaish, R. Szeliski, C. L. Zitnick, and S. B. Kang, "Reconstructing Occluded Surfaces using Synthetic Apertures: Stereo, Focus and Robust Measures," in *CVPR2006, Vol.II*, pp. 2331–2338, 2006.